Surface and Coatings Technology, Volume 517, December 2025, Article number 132844
DOI: 10.1016/j.surfcoat.2025.132844

Damage mechanisms in solid particle impact and erosion testing of thermal barrier coatings

Ben D. Beake[1,*], Luis Isern[2], Hannah Zhang[3], Christine Chalk[2], Stephen R. Goodes[1], Diane Johnson[2], Koldo Almandoz Forcen[2], John R. Nicholls[2] and Mark G. Gee[3]

1 Micro Materials Ltd., Willow House, Yale Business Village, Ellice Way, Wrexham, LL13 7YL, UK

2 Faculty of Engineering and Applied Sciences, Cranfield University, College Road, Cranfield, Bedfordshire, MK43 0AL, UK

3 National Physical Laboratory, Hampton Road, Teddington, Middlesex, TW11 0LW, UK

*Corresponding author: Tel: +44 1978 261615 (B.D. Beake); e-mail: ben.beake@micromaterials.co.uk (B.D. Beake)

Abstract

The ability of both cyclic and randomly spatially-distributed impact tests of columnar EB-PVD ceramic thermal barrier coating (TBC) systems with yttria stabilised zirconia (YSZ) and gadolinium zirconate (GZO) topcoats to simulate their behaviour in solid particle erosion tests has been investigated. The impact tests were able to replicate the main mechanisms and surface morphology in the erosion tests although there was more compaction in the impact tests. Densification below impact craters on YSZ and sub-surface cracking between the dense layer and the un-densified columns were revealed by focussed ion beam milling. Cracking over several columns and break-up of the columnar structure was observed in the impact and erosion tests on GZO. Clear differences in TBC erosion rate, with GZO being much less resistant to erosion, were replicated in the cyclic and randomly spatially-distributed micro-impact tests.

Keywords: Erosion, thermal barrier coating, impact, wear.

Published by Elsevier. This is the Author Accepted Manuscript issued with: Creative Commons Attribution License (CC:BY 4.0).
The final published version (version of record) is available online at DOI:10.1016/j.surfcoat.2025.132844. Please refer to any applicable publisher terms of use.

1. Introduction

Developing improved thermal barrier coating (TBC) systems is key to enabling higher engine operating temperatures that will increase the efficiency of gas turbines, saving fuel and reducing CO_2 emissions [1]. Development of particle impact resistant TBC systems continues to be a major development activity for a "prime-reliant" TBC [2]. Consideration of the mechanics of deformation by single particle impacts has led to improved understanding of TBC erosion processes [3-12]. In the hottest parts of the engine, the TBC topcoat is usually 7 wt.% yttria stabilised zirconia (7YSZ) deposited by Electron-Beam Physical Vapour Deposition (EB-PVD). Its erosion resistance is not particularly high, typically 2-3 times lower than the superalloy to which it is applied [12]. However, novel coating compositions with low thermal conductivity and high resistance to Calcia-magnesia-alumina-silicate (CMAS) attack, such as rare-earth zirconates, have been found to have even lower resistance to erosion. Darolia has noted that GE Aviation tested >200 TBC variants with altered microstructures and compositions finding, with a couple of exceptions, that they were unsuccessful in producing more erosion resistant TBCs [2]. Nano- and micro-mechanical test methods that can quickly and reliably simulate the main damage mechanisms that occur in solid particle erosion have the potential to solve this bottleneck by uncovering more details of the underlying relationships between erosion resistance, microstructure and mechanical properties in TBC systems. As an alternative to performing time-consuming erosion tests on every composition, the rapid nano-scale tests require only tiny volumes of material and enable many different novel coating compositions to be evaluated in a short time, potentially increasing the pace of coating development significantly and lowering its cost. Of these nanomechanical tests, the cyclic nano-impact test has been effective in the study of impact resistance at high strain rate and small scale. The tests are performed with a multifunctional nanomechanical test platform

(NanoTest Vantage) at strain rates that can approach 10^5 s^{-1}, several orders of magnitude higher than in quasi-static indentation [13].

Previous studies have investigated the correlation between coating performance in the cyclic impact test and erosion resistance [14-16] or performance in other repetitive contacts including discontinuous metal cutting applications such as end milling and interrupted turning [17-20]. When gas turbine engines operate under extreme conditions, hotspots can develop that cause localised sintering of the surface of the TBC [10]. Wellman and co-workers noted that thermal aging at 1100 °C and 1500 °C markedly increased the erosion rate of EB-PVD 7YSZ through sintering with a reduction in inter- and intra-column porosity [10]. Chen et al subsequently used nanoindentation to show that these heat treatments significantly increased the hardness and elastic modulus of the TBC [14]. The increased erosion rate for thermally aged TBCs was reproduced by greater damage in nano-impact tests performed with a diamond probe with 11.5 μm end radius. McMaster and co-workers reported a clear correlation between the relative ranking of DLC coatings on hardened steel in nano- and micro-impact tests and their resistance to sand erosion [15]. Venkatesh et al [16] investigated the behaviour of CrC-NiCr based coatings in nano-impact tests with a sharp cube corner indenter and in erosion tests (90°, 200 μm angular silica particles, 82 m/s). Laser clad, detonation sprayed and atmospheric plasma sprayed (APS) CrC-NiCr coatings with different microstructures were evaluated. They reported a good agreement between the nano-impact and solid particle erosion testing. The dominant damage mechanisms on each coating were reproduced in the impact test and a correlation between impact depth and mass loss observed.

In a cyclic impact test, the repetitive contact occurs at the same point on the surface. The impact depth is monitored throughout the test providing a convenient method for determining the number of impacts to failure in brittle materials [13]. A recently introduced test method for more closely replicating the statistical (apparently stochastic) distribution of multiple impacts

that occur in solid particle erosion is to perform cyclic controlled impacts at different locations on the sample surface [21,22]. In this new approach sample stage movement between impacts enables each impact to be at a new position. The novel technique provides a way to better understand microstructural and crack morphological influences on damage propagation at the single-impact level. In statistically distributed impact tests on glasses differences in the crack systems that develop under spherical impact were shown with predominantly radial-lateral cracking on BK7 glass and cone cracking on fused silica [22]. Experiments with controlled impact spacing showed that the radial-lateral system has a higher "critical interaction spacing" so that impacts spaced further apart interact causing greater material removal and a more rapid erosion rate for BK7.

In this study, we have investigated the impact and erosion behaviour of two EB-PVD ceramic thermal barrier coating systems with yttria stabilised zirconia (YSZ) and gadolinium zirconate (GZO) topcoats as baseline systems. With their unique columnar microstructure EB-PVD TBCs are much more strain tolerant than APS TBCs so are used on turbine blades in the hot gas stream where they are impacted by particles at higher velocities and angles thus making erosion resistance more critical [6]. For a TBC EB-7YSZ has relatively good erosion resistance [2]. GZO shows improved resistance to CMAS attack making the TBC less infiltrated in dusty turbine environments, has lower thermal conductivity, improved phase stability and bilayers with GZO top coats have a longer lifetime than YSZ in furnace cycling tests at 1100 °C [23]. However, GZO has reduced fracture toughness and erosion resistance has been reported to be significantly lower [23].

Small-scale wear test methods are most effective as screening tools to highlight promising coating compositions for further investigation when the major damage mechanisms that occur in the actual application can be accurately reproduced. In this study, we have performed 90° erosion tests with spherical and angular alumina particles and 90° impact tests with spherical

(R = 25 μm) and sharp (R ~100 nm) cube corner diamond probes. We investigated whether the differences in erosion resistance and the erosion damage mechanisms for the TBCs could be replicated in the impact tests, and the extent of quantitative agreement between the tests. Sub-surface deformation and cracking below the impact craters were investigated by FIB-milling through the craters and subsequent SEM imaging of the crater cross-sections. The similarities between damage caused by cyclic impacts at the same position and from statistically distributed impacts were compared. Impact tests with the spherical probe were also performed at 75° impact angle so that the influence of angle could be evaluated. Small-scale mechanical tests ideally require smooth surfaces to lower the effect of the surface roughness on the scatter of the results. In a previous study investigating the influence of aging on TBC behaviour, the surfaces were polished prior to nano-impact testing [14]. In this current work we have tested the TBCs as-deposited without any polishing.

2. Experimental

2.1 Coating Deposition

EB-PVD 7wt.% yttria stabilised zirconia (7YSZ) coating systems were produced with target thickness 180 μm 7YSZ top coat and 25 μm NiAl bond coat on Ni-Cr alloy (Nimonic 75) and sapphire substrates. EB-PVD gadolinium zirconate (GZO) coating systems were produced with a 175 μm top layer, 25 μm 7YSZ sub-layer and 25 μm NiAl bond coat on Ni-Cr alloy (Nimonic 75) and alumina substrates. The EB-PVD process used ingots of 7YSZ and GZO stoichiometry, O_2/10%Ar gas was added to counteract the dissociation of oxygen during evaporation. The pressure was kept constant at around 5 x 10^{-3} mbar and the temperature of the rotating substrates was kept at ~1000 °C. The NiAl bond coat was deposited by gas-phase aluminising (Chemical

Vapour Deposition, CVD) and the top coat by EB-PVD using a Von Ardenne EBE150 coating system both at Cranfield University.

Fig. 1(a-f) shows SEM images of top and side views of typical 7YSZ and GZO coatings. FIB sections in fig. 1(e-f) show that the columns are oriented normal to the surface on 7YSZ and at ~15° off from normal on the GZO. Surface roughness was determined from line scans in confocal microscopy (Olympus LEXT) images. The mean and standard deviation of the R_a surface roughness from 10 line scans over 640 μm of 7YSZ and GZO were (1.4 ± 0.1) μm and (0.9 ± 0.3 μm) respectively.

The TBCs were tested without polishing/any post-deposition treatment. Mechanical properties of the coatings have been reported previously [22] by spherical indentation tests at 1-10 N using a NanoTest Vantage (Micro Materials Ltd., Wrexham, UK). with 10 s loading, 10 s hold at peak load and 10 s unloading. There were 5 repeat tests at each load. The surface roughness had greater influence at lower loads where hardness was reduced (H ~30 % lower at 1 N than 10 N for both TBCs) although the elastic modulus was almost unaffected, varying little with depth. Mean values between 1-10 N, covering the depth range 5-30 μm were H = 1.9 ± 0.4 GPa, E = 84 ± 7 GPa for 7YSZ and H = 1.5 ± 0.2 GPa, E = 64 ± 6 GPa for GZO. The K_{1C} fracture toughness of 7YSZ has been estimated as 0.1-0.5 MPa $m^{1/2}$ [24]. The fracture toughness of GZO is around half of that of 7YSZ [25].

2.2 Nano- and micro-impact tests

Nano- and micro-impact tests were performed with a dual-loading head NanoTest Vantage, using its low (500 mN) and high (30 N) load heads respectively. For each impact the diamond indenter is withdrawn to a set distance above the sample surface and then rapidly accelerated to produce a high strain rate impact event. The impact energy and effective impact force can be controlled by varying the static load and/or the accelerating distance. For cyclic impact tests,

once the probe has come to rest it is retracted and reaccelerated to produce a pre-defined number of cyclic impacts at the same position on the surface. The impacts occur horizontally minimising the amount of debris remaining in the impact crater. Although experiments with an additional load cell placed behind the indenter have shown that dynamic forces in impact are significantly higher than the set forces, for convenience the results are described below using the set applied load.

Cyclic nano-impact tests at the same position were performed with a cube corner diamond indenter having an end radius close to 100 nm. The tests were performed at 10-50 mN applied load impacting at 90° to the surface, accelerating from 15 μm above the initial coating surface. The test duration was 200 s with 1 impact every 4 s, resulting in 50 impacts in total. There were 5 repeats at each load which were separated by 100 μm. Cyclic micro-impact tests at the same position were performed at 500-3000 mN applied load using a calibrated spheroconical diamond probe with 25 μm end radius and 90° cone angle impacting at 90° to the surface, accelerating from 50 μm above the initial coating surface. The test duration was 200 s with 1 impact every 4 s, resulting in 50 impacts in total. There were 3 repeats at each load which were separated by 250 μm. To perform cyclic impact tests impacting at 75° to the surface the TBCs were mounted on an angled sample holder. Tests at 75° were performed at 500-2500 mN on the 7YSZ and 500-1500 mN on the GZO. There were 3 repeats at each load which were separated by 250 μm. The micro-impact tests were performed on an instrument with a sensor having a 95 μm measurable displacement range. As the acceleration distance was set to 50 μm the maximum measurable impact depth during the tests was 45 μm.

Randomised (statistically distributed) micro-impact tests at 90° were set up using the same spheroconical probe used for the cyclic impacts at the same position with a programmed number (150) of statistically distributed impacts within 500 μm x 500 μm areas. After the tests

the probe geometry was rechecked by spherical indentation to confirm that no discernible probe wear had occurred. Tests were performed on both TBCs at 500 mN and accelerating distance of 50 μm with impact positions determined by programmed Gaussian and rectangular (i.e. equal probability of impacting anywhere within the test region) distributions. Figure 2 illustrates typical Gaussian and rectangular distributions. On the GZO samples additional tests at 1 N were performed with (i) a Gaussian distribution at 1 N (ii) two repeat tests at 1 N with the same rectangular distribution to assess reproducibility. Laser Scanning Confocal Microscopy (Olympus LEXT) was used to provide quantitative analysis of the material removed in the statistically distributed impact tests. For the cyclic impact tests in the same position the volume of material removed was estimated from the on-load depth after taking account of the test probe geometry, sample elastic recovery and frame compliance.

Each impact in the statistically distributed impact tests was analysed in the instrument software to determine the contact point, the maximum depth (h_{max}), residual depth (h_{res}), impact velocity V_{in} and rebound velocity V_{out}. From these the coefficient of restitution (e) and kinetic energy (KE) absorbed were determined and changes in these parameters with continued impact were investigated. An example (from a 1 N test on GZO) is shown in figure 3. The contact position ($h = 0$) was defined as the point of maximum velocity (V_{in}). The indenter penetrates the sample to a maximum depth, h_{max}. V_{out} is the maximum rebound velocity reached before the indenter leaves the surface, at h_{res}. The effective mass of the loading head, m, was determined by calibration following the approach detailed by Constantinides et al [26]. The effective mass was 240 g for the low load head used for the nano-impact testing and 4.8 kg for the high load head used for the micro-impact testing. The kinetic energy lost during impact is determined from

$$KE \text{ loss} = \tfrac{1}{2} m v_{in}^2 - \tfrac{1}{2} m v_{out}^2 \qquad \text{[Eqn. 1]}$$

The coefficient of restitution, e, is defined as

$e = | v_{out}/v_{in} |$ [Eqn. 2].

The KE loss ratio, λ, is equal to $1 - e^2$, and % dissipated energy = $100 * \lambda$.

Scanning electron microscopy (Tescan Vega) in back-scattered electron mode (BSE SEM) was used to image the impact craters.

2.3 Erosion testing

Erosion tests were performed at room temperature using the high-velocity erosion test facility at Cranfield University which has been described in detail previously [12]. It comprises a compressor supplying a pressure vessel, ensuring a constant supply of compressed air which passes through a convoluted path before entering the acceleration tube. The erodent is fed into the acceleration tube via a venturi nozzle, where compressed air accelerates the particles to impact the TBC surface [12]. The acceleration tube has a length of 1 m with an inner diameter of 12.7 mm and the nozzle to sample distance was 30 mm. The TBCs were impacted with an angle of attack of 90° (direction of particles perpendicular to TBC surface) with angular and spherical alumina particles at ~145 m/s (sieved 90-125 µm and d_{50}=112 µm respectively, from now on defined as erodent). The erodent rate was in all cases 4.6 g/min, weight change was evaluated at regular intervals of 30 s for 5 datapoints, increased to 60 s for at least 9 more datapoints, and increasing the period further until TBC failure was achieved. Repeat samples were used for each TBC material and set of conditions. TBC failure is defined as the first interval that displays a visible exposure of the bond coat.

2.4 Focussed Ion Beam (FIB) milling

A focussed ion beam was used to mill sections through the TBCs to study sub-surface structure and damage due to impact/erosion. A Tescan Solaris X with a Xe plasma FIB source was used

to mill the bulk trench structures in the sample surface with the focused ion beam using an accelerating voltage of 30 keV and beam current of 100 nA, these trenches were of slightly varied dimensions but generally in the size region of 60-100 x 50-60 x 50-80 μm. The final ion beam polishing of the trench face was performed using a Tescan S8000 with Ga Liquid Ion Metal FIB Source at an accelerating voltage 30keV and 20 nA followed by a final milling stage at 10 nA, as this gave a better defined, defect free final cross section than the Xe plasma. These milled trench structures enabled the electron beam to be scanned across cross section trench viewing the subsurface structures by producing secondary and backscattered images revealing the depths and structures of the subsurface components. Sections were milled through (i) unmodified 7YSZ and GZO to reveal the columnar structure and through the centre of (ii) a 500 mN cyclic impact crater on 7YSZ and (iii) a 3 N cyclic impact crater on 7YSZ and (iv) 500 mN random impact tests on GZO to investigate sub-surface deformation and cracking.

3. Results

3.1 Cyclic nano-impact tests

Typical impact depth vs. number of impacts curves at 5-50 mN are shown for 7YSZ in fig. 4(a) and for GZO in fig. 4(b). For both TBCs there was a generally gradual increase in depth with continued impacting. In some tests the gradual increase in depth was interrupted by an isolated depth decrease of ~0.5-1 μm, as can be seen in fig. 4 after 7 impacts on GZO at 5 mN or after 11 impacts on 7YSZ at 20 mN. 80% of tests showed a depth decrease, although many were much smaller. The variation in the initial impact depth (after the first impact), and the final impact depth, are shown in figs. 4(c) and (d) respectively. The final impact depths were generally higher on GZO although there was considerable scatter in the results due to the high surface roughness of both TBC.

3.2 Cyclic micro-impact tests at 90°

Typical impact depth vs. number of impacts curves are shown for 7YSZ in fig. 5(a) and for GZO in fig. 5(b). Occasional downward depth steps were seen in the majority of curves on GZO but were never observed on 7YSZ. The variation in the initial and final impact depths are shown in figs. 5(c) and (d) respectively. Initial impact depths are larger on GZO and differences with 7YSZ grow with continued impacts. At 2500 and 3000 mN the depth on GZO exceeded the maximum available depth range of the test instrument used before the end of the tests so the values reported in fig. 5(c) are lower bounds.

Illustrative SEM images of impact craters are shown in figure 6. For all the tests the final impact crater size extended across several columns. The top-view images (fig. 6(a,b)) show that, with the spherical probe in the cyclic tests on 7YSZ, the deformation was dominated by compaction, squashing the tips of the columns with some localised cracking around the periphery of each crater. On GZO there was also compaction, but this was associated with more extensive cracking at the periphery and in several tests, even at the lowest load, there was debris present within the impact craters (fig. 6c,d). There was also cracking in the bottom of the crater, especially at higher load on GZO.

Figure 7 shows images after FIB-milling through cross-sections through impact craters on 7YSZ at (a,b) 500 mN and (c,d) 3000 mN. There is a lighter compacted region extending around 5-15 μm below the impact craters within which no cracks can be observed. At 500 mN cracks formed at or close to the boundary between the compacted region and the region immediately below it, and extended over several columns. Damage at 3000 mN was more extensive with several areas where the columnar structure appears to be broken up into very small fragments.

3.3 Cyclic micro-impact testing at 75°

Figure 8 compares typical 500 mN and 1500 mN impact depth vs. number of impacts curves at 75° with typical curves at 90° impact. On 7YSZ (fig. 8(a)) the curves were almost indistinguishable for the two angles. On GZO (fig. 8(b)) they were initially identical at both angles but then started to deviate from each other from ~8 impacts, with the impact damage at 75° being much reduced and the small downward depth steps are absent. Fig. 8(c) shows comparative final impact depth data on both TBCs at 75° and 90°. In the 75° tests on GZO the cracking zone at the periphery was less wide than in the 90° tests. The debris inside the impact craters was only observed in a couple of tests. Comparative images on both TBCs at 1500 mN and both angles are shown in figs. 8(d)-8(g).

3.4 Statistically distributed micro-impact tests

Laser scanning confocal images of the 150-impact random impact experiments at 500 mN are shown in fig. 9. The tests with Gaussian and rectangular distributions on 7YSZ are shown in figs. 9(a) and 9(b) respectively. The tests with Gaussian and rectangular distributions on GZO are shown in figs 9(c) and 9(d) respectively. Fig. 9(e,f) shows the programmed impact positions on GZO overlaid on the confocal images from figs. 9(c) and 9(d) respectively. Comparing the images in figs. 9(a-d) it can be seen that 7YSZ was significantly more resistant to impact damage than GZO. With a Gaussian distribution there was greater damage near the central point on 7YSZ. On GZO (fig. 9(c,d)) there was an extensive region with more material removal in the tests with rectangular and Gaussian distributions. Laser scanning confocal images of the 150-impact random impact experiments on GZO at 1000 mN are shown in figure 10. In comparison to the tests at 500 mN the central region with greater coating loss extended further over the test region. Fig. 10(c) shows laser scanning confocal microscopy and fig 10(d) BSE SEM images of the test on GZO with a Gaussian distribution. A higher resolution BSE SEM image of the central region is shown in fig. 10(e). The columnar structure has been completely

broken down into fine-scale fragments. There is evidence of fracture in the base of some impact craters. Table 1 shows the volume lost determined from the laser scanning confocal measurements.

Table 1. Impact volume after 150 impacts

TBC	Load (mN)	Distribution type	Volume (μm^3)	% severely fractured area
7YSZ	500	Rectangular	93,800	0
7YSZ	500	Gaussian	141,100	2
GZO	500	Rectangular	200,600	16
GZO	500	Gaussian	410,800	29
GZO	1000	Rectangular	2,340,000	52
GZO	1000	Rectangular	2,571,800	57
GZO	1000	Gaussian	1,159,200	39

The variation in final depth with number of impacts in the tests on GZO is shown for 500 mN and 1000 mN in fig. 11(a) and (b) respectively. At both loads the transition to a more severe damage regime occurred more quickly in the tests with the Gaussian distribution. In the Gaussian distribution test at 1 N the more severely damaged region extended over less of the test area than for the rectangular distributions, resulting in a lower wear volume.

The coefficient of restitution (e) provides a measure of the elasticity of the impact (for perfectly elastic collisions $e = 1$ and perfectly plastic collisions $e = 0$). This parameter was not particularly sensitive to the transition to the more severe wear regime during the tests. For example, mean values of e in the tests at 500 mN with Gaussian distribution were (0.32 ± 0.04) on 7YSZ and (0.34 ± 0.02) on GZO. Mean values of e were 0.3-0.35 in all the other tests. The

kinetic energy absorbed was more sensitive to the transition to more severe wear. Fig. 11(c) shows the *KE* absorbed for the tests on GZO at 500 and 1000 mN with Gaussian distributions.

3.5 Erosion testing

Fig. 12 shows the mass loss results from 2 repeat erosion tests on the TBCs with (a) angular and (b) spherical alumina particles. The steady-state erosion rate (ER) in both tests is around 6 times higher for GZO, 4.9±0.0 g/kg for 7YSZ vs 32.3±1.2 g/kg for GZO using angular particles, and 6.6±0.2 g/kg 7YSZ vs 41.2±0.8 g/kg for GZO using spherical particles.

SEM images of cross-sections of the eroded 7YSZ show evidence of cracking between columns in the tests with angular (fig. 13(a,b) and spherical (fig. 13(c)) alumina erodent. Near the region where the coating has spalled off there is evidence of a more severe damage mode with complete destruction of the columnar structure.

Fig. 14(a) shows the top-surface of GZO eroded by angular alumina. The GZO surface appeared similar after spherical and angular alumina erosion. The top surface of 7YSZ at the edge of the eroded region (fig. 14(b) and (c)), where the impact density was lower, shows evidence of compaction with the tops of the columns squashed, accompanied by some fracturing.

4. Discussion

TBCs are erosion tested without any post-deposition surface treatment. For erosion simulation, it is desirable to be able to perform nano- and micro-impact tests on the TBCs without the need for surface polishing prior to testing, which could lead to significant coating thickness removal [27] and/or unwanted modification of the mechanical properties. Therefore, notwithstanding their high surface roughness, the TBCs were tested as-deposited in this study. The high surface

roughness of the TBCs and its columnar microstructure resulted in considerable scatter in the low load nano-impact measurements with the sharp cube corner probe. With this sharp probe the initial contact may be on a column top or between columns. Nicholls and Wellman have used the D/d ratio (contact diameter/column diameter) to differentiate between different erosion regimes [5-7,9-11]. The contact footprint (D) in the nano-impact tests is initially smaller than the column diameter (d) for the lower loads (D/d <1). The variability in the tests therefore might reflect whether the probe hits on the top of a column or at an intersection between two or more columns. For this reason, there was no difference between the TBCs in their initial impact behaviour at low load. As the test progresses, the contact zone becomes larger and differences between them begin to emerge. The TBCs showed a predominantly brittle response to nano-impact with occasional isolated depth decreases of around 500 nm during the test. These decreases have been observed previously in nano-impact tests on brittle zirconia coatings on glass [28] where they were interpreted as uplift/blistering due to cracking, and in other materials such as hard nitride coatings on cemented carbide where they mark the transition to a subsequent more rapid removal rate [13]. On the TBCs, there is no increase in damage rate after their occurrence and they are more likely to be due to brittle impact debris created at the edge of the crater falling into the impact crater, as witnessed in figure 6. The parameter (h_f-h_1) has been used previously [29] to focus on damage after initial impact, enabling comparison between tests at different loads, or for thin coatings deposited on substrates with different load support. Switching focus from the maximum depth in the nano-impact test to the change in depth after the initial impact h_f-h_1 also appears to be a useful way of mitigating the effect of high surface roughness in TBCs.

In the micro-impact tests, the influence of the surface roughness was significantly reduced as the impact depth is larger and D/d >1. Part of the reason for the initially lower impact depth on 7YSZ in the micro-impact tests is likely to be that it is slightly harder and stiffer than GZO.

Differences between them increase with continued impact. The improved performance of 7YSZ in the cyclic micro-impact tests is consistent with its higher fracture toughness [2,24,25]. Impact resistance and toughness are correlated in YSZ, with peak toughness reported around 4 wt.% yttria and peak impact resistance around 3 wt.% yttria [2]. The angled columns in GZO might be another factor contributing to its lower impact resistance. Wellman and co-workers have shown that 7YSZ coatings produced with angled columns display higher erosion rate [10].

Performing the impact tests at 75° had different effects on the two TBCs. At 75°, GZO showed very few of the depth steps that occur under 90° impact and its behaviour was closer to that of 7YSZ with more compaction and less fracture. The greater impact resistance at 75° for GZO is connected to its high brittleness. Maximum erosion damage typically occurs for brittle materials at 90° impact [7,30-33] although there can be relatively little difference between 75° and 90°. For example, Chen and co-workers investigated the angle dependence of erosion rate for 12 μm TiN/ZrN nanomultilayered coating on Ti6Al4V [34]. The maximum erosion rate was at 90°, approximately 3.1, 2.8 and 1.2 times larger than at 15°, 45° and 75°. Yang and McKellar reported that increasing the number of layers in multilayered CrAlTiN-AlTiN changed the relative erosion rate at 30 and 90°; with more layers the coatings were no longer eroded at a higher rate at 90° [35], and nanolayered CrAlTiN showed higher erosion at 30°, indicating higher toughness with more interfaces. Sheldon and Finnie [36] showed that, for glasses and ceramics that are usually considered as brittle materials, the maximum erosion rate was not always at 90° and the angle at which maximum erosion occurred varied with the size of the erodent particles. Subsequently, this effect was shown to be due to a transition from brittle fracture-dominated behaviour with large particle sizes to plasticity-dominated behaviour for smaller particles [31,32,37]. On EB-TBC and APS 7YSZ, Nicholls and co-workers showed

a sigmoid relationship between impact angle and the relative erosion rate (erosion rate/erosion rate at 90°) with little change in erosion rate between 75° and 90° although the best-fit peak erosion rate being around 75 to 80° [7,38]. Modelling [7,33] indicates little change in ER between 75° and 90°, with a maximum at 90°. When eroding at glancing angle, only the vertical component contributes to cracking although the horizontal component could contribute to removal of columns that have been cracked [7]. In the impact tests on 7YSZ there was less fracture and more compaction which could be consistent with this. Sub-surface damage investigated by FIB cross-sections through impact craters is discussed later.

The on-load impact depth data has been converted to impact volume by taking account of probe geometry, elastic recovery and instrument frame compliance contribution. After the conversion to volume there was a linear relationship between the initial impact depth and the applied load (R^2 = 0.995 on 7YSZ) (fig. 15(a)). There was a linear load dependence between the applied load and the final impact volume to 2 N on 7YSZ and to 1.5 N on GZO (fig. 15(b)). Above these loads there was deviation from linearity on both TBCs, with the impact volume increasing with load at a lower rate. Possible reasons for this on GZO include (i) not taking into account material removal outside the crater through cracking at the periphery (ii) debris failing into crater (iii) influence of harder 7YSZ sub-layer (iv) non-linearity of the relationship between the set and actual force at higher load as separate experiments with a load cell have shown that the F_{actual}/F_{set} is lower for loads >2 N.

SEM images show that the initial impact is compaction dominated and flattens the tops of the columns [22]. The LEXT images and the in-situ test metrics such as *KE* absorbed show that a transition to a more severe damage mechanism occurs on GZO. In the regions where the LEXT images show more material is removed, SEM images show a transition to smaller-sized debris fragments. Interestingly, the erosion rate at the start of the tests on GZO shows a stronger incubation period with lower erosion than on 7YSZ, although the value of this GZO's transitory

erosion rate is still higher than 7YSZ's. This difference may be due to higher particle embedment before the steady state is reached on GZO.

Reproducing erosion damage mechanisms

Small-scale wear test methods are most effective as screening tools for promising compositions when the major damage mechanisms that occur in the actual application can be reproduced. For TBCs Wellman and Nicholls have produced an erosion map showing the relationship between particle size, velocity (which control the impact energy) and erosion regime [7,11]. The kinetic energies in the nano- and micro-impact tests have been calculated and compared to the kinetic energies of the individual impacts in the erosion tests. For impact at 145 m/s by spherical alumina particles of radius = 56 μm and density 4000 kg/m^3 this equates to an impact energy of 31 μJ. They lie within the Mode I regime of small particle erosion involving near-surface cracking and lateral cracking. In the nano-impact tests produced with the low effective mass load head the kinetic energies are somewhat lower than this. However, the micro-impacts produced with the high load head having a much higher 4.8 kg effective mass are broadly comparable. For example, at 500 mN accelerating from 50 μm above the surface the typical velocity on contact is 4.2 mm/s which equates to an impact energy of 42 μJ, or around 40 % higher than the mean erosion impact energy. Nicholls and Wellman also subsequently used the D/d ratio (contact diameter/column diameter) to differentiate between Mode I small particle erosion (cracking, D/d <2), Mode II compaction damage (D/d, 2-12), Mode III foreign object damage, (D/d > 12) erosion mechanisms in TBCs [7,10,11]. In the nano-impact tests, the sharp cube corner probe and low initial impact depths give D/d ~1 for the lowest loads. With the larger probe radius used in the micro-impact tests D/d was initially ~3 at the lowest loads consistent with the compaction seen in the SEM images. However, in the impact tests there is some cracking at the edges (even of single impacts) so the spherical impacts could be considered as primarily Mode I combined with some Mode II character.

In Mode I, damage is limited to the near-surface and cracking typically occurs at 10-20 μm depth. This is supplemented by some more extensive cracking causing break-up of the columnar structure. Chen et al [3] have noted that in high temperature erosion a shallow densified zone around 1-5 μm deep can be formed by successive impacts. Subsequent impacts induce stress concentrations at the transition between the dense layer and the underlying columns which cause cracking at the transition point between the layer and the rest of the TBC resulting in the removal of material above this. At elevated temperature the yield stress of the TBC decreases [3,25] so the TBC is easier to densify. The formation of the dense layer in TBC erosion bears some similarities to the formation of a brittle white layer in erosion of steels where multiple impact builds up plastic strain to produce a harder tribologically transformed structure layer (TTS) [39].

In cyclic nano-impact tests of alumina and partially stabilised zirconia ceramics, sub-surface cracking was observed below nano-impact craters [40]. Finite element modelling of multiple impacts on bulk SiC distributed within a set region by Wang and Yang also showed sub-surface cracking [30]. Chen et al have previously suggested that cracks form near surface due to returning elastic waves causing stress concentrations at that point [3]. The generality of sub-surface cracking would argue against this idea. Hutchings noted that only a small fraction of the energy of an impact is in the form of elastic waves, typically ~1-5 % [41,42]. Under the conditions in the micro-impact tests the % dissipated energy was usually close to 90 % for both TBCs and was relatively insensitive to whether there was a transition to more extensive fracture in the test. For example, the mean % dissipated energy in the 150 impacts in the 500 mN tests on GZO with Gaussian distribution was (88.4 ± 1.2) %.

In the cyclic impact test with the spherical probe there is more compaction than in true Mode I small particle erosion but nevertheless the mechanism appears very similar. Figure 7 clearly shows that the densified layer with sub-surface cracks forming at the intersection of the dense

layer and the un-densified columns, and some additional cracking along the column boundaries. The magnitude of the developed stresses in impact and the position of the von Mises (plasticity) stress maximum below the surface can be estimated from analysis of the impact depth data, for the spheroconical indenter. This analysis shows that large stresses develop below the impact zone, above the yield stress of the TBC, consistent with the presence of the layer of densified/compacted material in the SEM images of the FIB-milled craters. The maximum von Mises stresses were initially around 10 μm below the surface, consistent with the size of the densified zone, and the typical crack depths of 10-15 μm below the surface. Wellman and Nicholls noted that mode II has the effect of densifying the near surface of the coating, conditioning the TBC for later material removal, e.g. through small particle erosion [11]. The SEM images of FIB-milled craters in figure 7 are consistent with this interpretation.

Although top views of cyclic impact craters on 7YSZ (e.g. fig. 6a,b) show little differences in mechanism with load, the FIB-milled sections show the median/lateral cracking seen in the eroded samples (fig. 13(a,b)), and in previous studies [6]. Since the predominant cracking is parallel to the surface Wellman and Nicholls [6] proposed a mechanism where (i) on initial loading a region of inelastic deformation (possibly densification) forms surrounded by elastic deformation (ii) on unloading the elastic region is prevented from relaxation due to constraint from the inelastic region (iii) there is resultant tensile stress and cracks initiate parallel to the surface. The 7YSZ TBC has ~50% of the theoretical density so inelastic deformation is likely to be densification (compaction) of the columns [6].

SEM images of the GZO surface (figs. 10(d,e) and 14(a)) show very similar fine-scale debris from complete break-up of the columns after erosion and micro-impact tests. We have previously shown that the columnar structure on GZO is broken into progressively smaller fragments by continued impacts [22] and that only the craters left by the final impacts are observed since most of the previous impact craters are covered by impact debris. By overlaying

the distributions of the impacts against the LEXT images (figs. 9(c,d)), it can be seen that, although the heavily fractured areas can be associated with higher impact densities, there are also fractured areas with little/no impacts in the vicinity. The 500 mN rectangular distribution test on GZO shown in figure 9(d) is an example. There are heavily fractured regions where the nearest impact site was >50 μm away which indicates cracking from one column is extending over several columns (i.e. the same major material removal mechanism as in erosion). FIB-milled sections through damaged regions in randomly spatially-distributed impact tests at 500 mN on GSZ (fig. 13(c)) also show the sub-surface cracking across several columns and detachment. SEM images of the edge of the eroded region on 7YSZ where the impact density is much lower show some compaction and flattening of the tops of the columns (fig. 14(b,c)) as is observed in the micro-impact tests.

Quantification of differences in TBC impact resistance and erosion rate

Linear fitting to the data for volume of material removed at the end of the nano- and micro-impact tests vs. the applied load was used as an estimate of erosion rate. The volume of material removed in cyclic micro-impact tests was lowest for 7YSZ at 90° impact, and was a factor of 2.2 higher for GZO under the same conditions. For YSZ there was around 10% more material removal at 75° impact than at 90°. For 75° GZO there was around 50% less material removal at 75° impact than at 90°, with these differences in angle dependence being consistent with the GZO being more brittle. In the statistically distributed tests at 500 mN GZO was a factor of 2.1 worse than 7YSZ in the rectangular distribution and a factor of 2.9 worse in the test with a Gaussian distribution. In the nano-impact tests GZO was a factor of 1.9-3.3 less erosion resistant than 7YSZ although due to the larger effect of the high surface roughness at smaller length scale the volume calculation has higher uncertainty with more scatter and a less obvious linear fit. The same approach to estimate impact volume from depth data has been applied to the nano-impact data of Venkatesh and co-workers on chromium carbide-based coatings [16].

Given the scatter in impact data, there was reasonable quantitative agreement with the erosion data. The relative ER varied 1:1.2:1.6 from detonation sprayed coating, laser clad, and plasma sprayed coatings, whilst comparative impact volumes estimated from the probe depths varied in the ratio 1:1.3:2.8, although there was considerable experimental scatter for the less erosion resistant plasma sprayed coating.

In the erosion tests on the TBCs, the steady state ER was around 6 times higher on GZO with both the spherical and angular alumina erodent. However, differences between the TBCs during the incubation period at the start of the erosion tests before the steady state region was reached were smaller (~3 in the spherical and ~3-4 in the tests with the angular alumina). These initially lower erosion rates and smaller difference between the TBCs may in part be due to particle embedment but also may have a component from the greater compaction. A similar increase in erosion rate between the initial and steady-state rate was observed in the micro-impact test. The initial volume loss in the cyclic micro-impact tests was a factor of 1.8 higher for GZO than 7YSZ due to a combination of plasticity (compaction) and cracking. Cracking becomes more important with continued impact and the difference between GZO and 7YSZ widens. The lower ER in the impact tests compared to the erosion tests is likely to be a consequence of the greater compaction in the impact test. It is worth noticing that the similar density of 7YSZ and GZO (difference ~5%) enables a direct comparison of mass loss with volume loss.

Future outlook

The test is quick and easy to run and has considerable potential as a screening test for coatings. Although not strictly quantitative in terms of the absolute magnitude of ER differences (presumably due to the greater compaction under the impact test conditions), the mechanistic features of the impact damage were well reproduced in the micro-impact tests and relative differences between coatings should be reliable. Different probe geometries, impact angles and

load levels enable mechanistic transitions to be studied in detail. Further optimisation of the impact parameters could adjust the compaction vs. cracking ratio.

Erosion tests typically have some uncertainty and variability in the erosion rate. The possibility to run repeat tests with exactly the same spatial distribution (as was done in this study in the two repeat tests at 1 N on GZO) would be beneficial in lowering the uncertainty. The same spatial distribution of impacts could be run on multiple samples and/or across a range of loads, as has been done elsewhere on hard PVD coatings [43]. The experimental results described in this study could be supplemented by finite element or analytical models of multiple impacts, as has been done for EB-PVD TBCs for a single impact [3-5,44] or a few impacts on other materials systems [30,36]. With the current setup using spheroconical probes, the maximum angle off normal is limited before contact would not be in the spherical end cap. To allow higher impact angles whilst remaining within the spherical, an offset indenter mount has been designed. Performing micro-impact tests on TBCs at elevated temperatures could be a reliable and convenient approach for simulating high temperature erosion. Preliminary micro-impact tests with a R = 25 μm spherical probe have been performed on 7YSZ at 500 and 850 °C [45].

5. Conclusions

The impact tests were able to replicate the main mechanisms and surface morphology in the erosion tests although there was more compaction in the impact tests, which may be due to differences in erodent/probe geometry. Densification below impact craters on 7YSZ and sub-surface cracking between the dense layer and the un-densified columns were revealed by focussed ion beam milling. Cracking over several columns and break-up of the columnar structure was observed in the impact and erosion tests on GZO. Clear differences in TBC erosion rate, with GZO being much less resistant to erosion, were replicated in the cyclic and

statistically distributed micro-impact tests. The major erosion damage mechanisms were reproduced in the cyclic and statistically distributed micro-impact tests so these should have considerable potential as screening tests for evaluating promising erosion-resistant TBC compositions.

Acknowledgements

Support from Innovate UK under Smart Award project #10020751, High temperature tools for designing sustainable erosion resistant coatings, is gratefully acknowledged.

References

1. D.R. Clarke, M. Oechsner and N.P. Padture, Thermal-barrier coatings for more efficient gas-turbine engines, MRS Bull. 37 (2012) 891-898.
2. R. Darolia, Thermal barrier coatings technology: critical review, progress update, remaining challenges and prospects, Int. Mater. Rev. 58 (2013) 315-348.
3. X. Chen, M.Y. He, I. Spitsberg, N.A. Fleck, J.W. Hutchinson, A.G. Evans, Mechanisms governing the high temperature erosion of thermal barrier coatings, Wear 256 (2004) 735-756.
4. A.G. Evans, N.A. Fleck, S. Faulhaber, N. Vermaak, M. Maloney, R. Darolia, Scaling laws governing the erosion and impact resistance of thermal barrier coatings, Wear 260 (2006) 886-894.
5. T. Zisis, N.A. Fleck, The elastic-plastic indentation response of a columnar thermal barrier coating, Wear 268 (2010) 443-454.
6. R.G. Wellman, J.R. Nicholls, Some observations on erosion mechanisms of EB-PVD TBCs, Wear 242 (2000) 89-96.
7. R.G. Wellman and J.R. Nicholls, A mechanism for the erosion of EB PVD TBCs, Mater. Sci, Forum, 369-372 (2001) 531-538.
8. R.G. Wellman and J.R. Nicholls, Nano and Micro indentation studies of bulk zirconia and EB PVD TBCs, Surf. Coat. Technol. 176 (2004) 253-260.
9. J.R. Nicholls and R.G. Wellman, Erosion and foreign object damage of thermal barrier coatings, Proc. RTO AVT, "The control and reduction of wear in military platforms", Williamsburg, USA, 2003 published as Nato report RTO-MP-AVT-109-20 (2004).
10. R.G. Wellman, M.J. Deakin, J.R. Nicholls, The effect of TBC morphology on the erosion rate of EB PVD TBCs, Wear 258 (2005) 349-356.
11. R.G. Wellman and J.R. Nicholls, A review of the erosion of thermal barrier coatings, J. Phys. D: Appl. Phys. 16 (2007) R293-R305.
12. R.G. Wellman, J.R. Nicholls, K. Murphy, Effect of microstructure and temperature on the erosion rates and mechanisms of modified EB PVD TBCs, Wear 267 (2009) 1927-1934.
13. B.D. Beake, Nano- and micro-scale impact testing of hard coatings: a review, Coatings 12 (2022) 793.
14. J. Chen, B.D. Beake, R.G. Wellman, J.R. Nicholls, H. Dong, An investigation into the correlation between nano-impact resistance and erosion performance of EB-PVD thermal barrier coatings on thermal ageing, Surf. Coat. Technol. 206 (2012) 4992-4498.
15. S.J. McMaster, T.W. Liskiewicz, A. Neville, B.D. Beake, Probing fatigue resistance in multi-layer DLC coatings by micro- and nano-impact: Correlation to erosion tests, Surf. Coat. Technol. 402 (2020) 126319.
16. L. Ventakesh, S.B. Pitchuka, G. Sivakumar, R.C. Gundakaram, S.V. Joshi, Microstructural response of various chromium carbide based coatings to erosion and nano impact testing, Wear 386-387 (2017) 72-79.
17. K.-D. Bouzakis, F. Flocke, G. Skordaris, E. Bouzakis, S. Geradis, G. Katirtzoglou and S. Makrimallakis, Influence of dry micro-blasting grain quality on wear behaviour of TiAlN coated tools, Wear 271 (2011) 783-791.
18. G. Skordaris K.-D. Bouzakis, P. Charalampous, E. Bouzakis, R. Paraskevopoulou, O. Lemmer, S. Bolz, Brittleness and fatigue effect of mono- and multi-layer PVD films on

the cutting performance of coated cemented carbide inserts, CIRP Annals - Manuf Tech 63 (2014) 93.
19. G. Skordaris, K.D. Bouzakis, T. Kotsanis, P. Charalampous, E. Bouzakis, B. Breidenstein, B. Bergmann, B. Denkena, Effect of PVD film's residual stress on their mechanical properties, brittleness, adhesion and cutting performance of coated tools, CIRP. J. Manufact. Sci. Technol. 18 (2017) 145-151.
20. B.D. Beake, J.F. Smith, A. Gray, G.S. Fox-Rabinovich, S.C. Veldhuis, J.L. Endrino, Investigating the correlation between nano-impact fracture resistance and hardness/modulus ratio from nanoindentation at 25-500ºC and the fracture resistance and lifetime of cutting tools with Ti1-xAlxN (x=0.5 and 0.67) PVD coatings in milling operations, Surf. Coat. Technol. 201 (2007) 4585.
21. UK Patent GB2624893Surface Testing Apparatus; filed 29/11/22; granted 10/12/24.
22. B.D. Beake, S.R. Goodes, H. Zhang, L. Isern, C. Chalk, J.R. Nicholls, M.G. Gee, Randomised nano-/micro- impact testing – a novel experimental test method to simulate erosive damage caused by solid particle impacts, Tribol. Int. 195 (2024) 109647.
23. U. Schulz, A. Nowotnik, S. Kunkel, G. Reiter, Effect of processing and interface on the durability of single and bilayer 7YSZ / gadolinium zirconate EB-PVD thermal barrier coatings, Surf. Coat. Technol. 381 (2020) 125107.
24. X. Geng, R. Wellman, L. Isern, C. Chalk, Estimation of thermal barrier coating fracture toughness using integrated computational materials engineering, Ceram. Int. 49 (2023) 25788-25794.
25. S. Mahade, N. Curry, S. Björklund, N. Markocsan, S. Joshi, Durability of Gadolinium Zirconate/YSZ double-layered thermal barrier coatings under different thermal cyclic test conditions, Materials 12 (2019) 2238.
26. G. Constantinides, C.A. Tweedie, N. Savva, J.F. Smith, K.J. Van Vliet, Quantitative impact testing of energy dissipation at surfaces, Exp. Mech. 49 (2009) 511–522.
27. C.-H. Kim, A.H. Heuer, A high-temperature displacement-sensitive indenter for studying mechanical properties of thermal barrier coatings, J. Mater. Res. 19 (2004) 351-356.
28. B.D. Beake, L. Isern, D. Bhattacharyya, J.L. Endrino, K. Lawson, T. Walker, Nano- and micro-scale impact testing of zirconia, alumina and zirconia-alumina duplex optical coatings on glass, Wear 462-463 (2020) 203499.
29. B.D. Beake, L. Isern, J.L. Endrino, T.W. Liskiewicz, X. Shi, Micro-scale impact resistance of coatings on hardened tool steel and cemented carbide, Mater. Lett. 284 (2021) 129009.
30. E. Bousser, L. Martinu, J.E. Klemberg-Sapieha, Solid particle erosion mechanisms of protective coatings for aerospace applications. Surf. Coat. Technol. 257, (2014) 165-181.
31. I.M. Hutchings, Transitions, threshold effects and erosion maps, Key Eng. Mater. 71 (1992) 75-92.
32. I.M. Hutchings, Ductile-brittle transitions and wear maps for the erosion and abrasion of brittle materials, J. Phys. D: Appl. Phys. 25 (1992) A212.
33. Y.-F. Wang, Z.-G. Yang, Finite element model of erosive wear on ductile and brittle materials, Wear 265 (2008) 871-878.

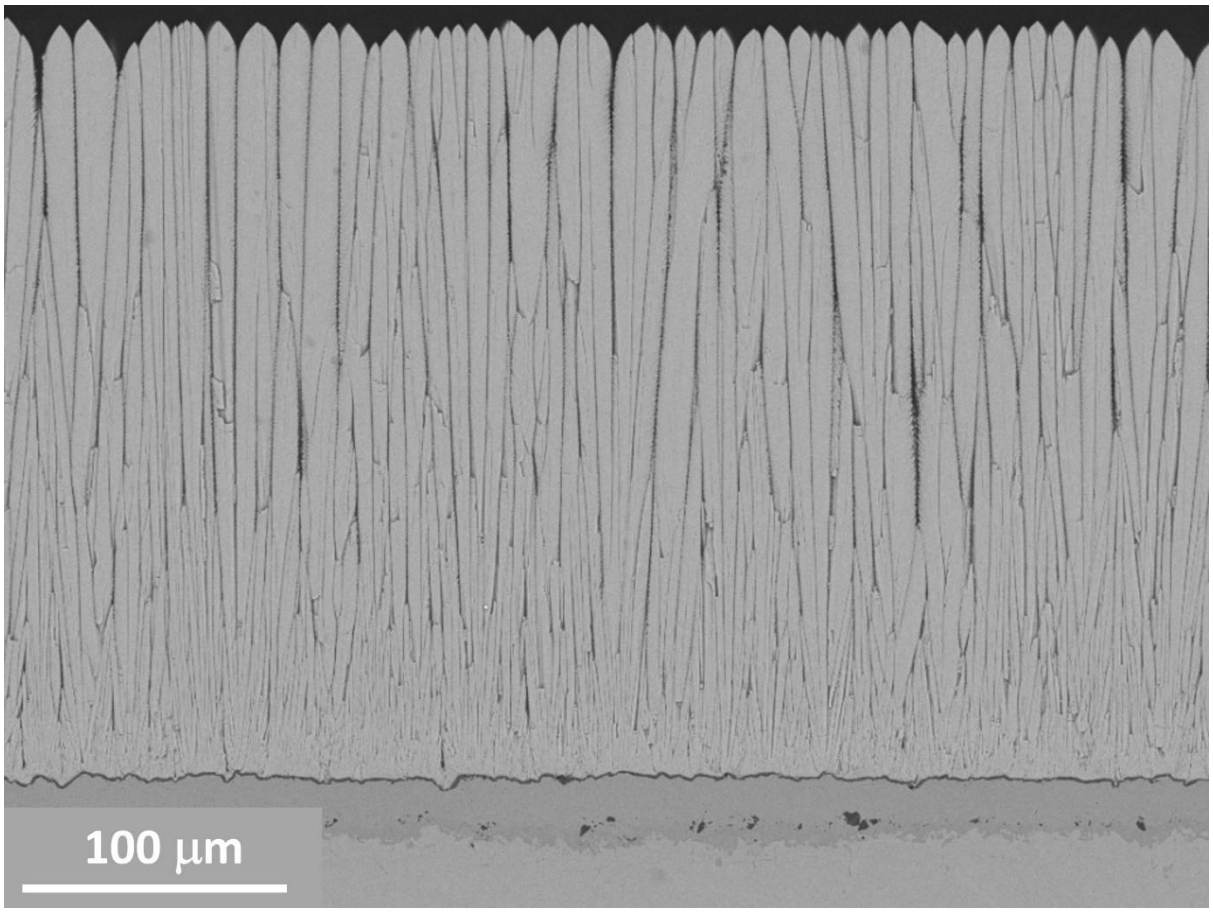
34. J. Chen, Z. Zhang, G. Yang, Z. Fang, Z. Yang, Z. Li, G. He, Performance and damage mechanism of TiN/ZrN nano-multilayer coatings based on different erosion angles, Appl. Surf. Sci. 513 (2020) 145457.
35. Q. Yang, R. McKellar, Nanolayered CrAlTiN and multilayered CrAlTiN-AlTiN coatings for solid particles erosion protection, Tribol. Int. 83 (2015) 12-20.
36. G.L. Sheldon, I. Finnie, On the ductile behaviour of nominally brittle materials during erosive cutting, Trans. ASME B (J. Eng. Ind.), 88B (1966) 387-292.
37. H. Wensink, M.C. Elwenspoek, A closer look at the ductile-brittle transition in solid particle erosion, Wear 253 (2002) 1035-1043.
38. J.R. Nicholls, Y. Jaslier, D.S. Rickerby, Erosion of EB-PVD thermal barrier coatings, Materials at High Temperatures 15 (1998) 15-22.
39. V. Javaheri, S. Sadeghpour, P. Karjalainen, M. Lindroos, O. Haiko, N. Sarmadi et al., Formation of nanostructured surface layer, the white layer, through solid particles impingement during slurry erosion in a martensitic medium-carbon steel, Wear 496-497 (2022) 204301.
40. B.D. Beake, R. Ctvrtlik, A.J. Harris, A.S. Martin, L. Vaclavek, J. Manak, V. Ranc, High frequency acoustic emission monitoring in nano-impact of alumina and partially stabilised zirconia, Mater. Sci. Eng. A 780 (2020) 139159 (11pp).
41. I.M. Hutchings, A model for the erosion of metals by spherical particles at normal incidence, Wear 1981.
42. I.M. Hutchings, Energy absorbed by elastic waves during plastic impact, J. Phys. D: Appl. Phys. 12 (1979) 1819-1824.
43. B.D. Beake, J. Roberts, Y. Zhu, T.W. Liskiewicz, Simulating erosion tests with statistically distributed micro-scale impact: a study on PVD TiAlN and AlCrN coatings, Wear 570 (2024) 205911.
44. Z.S. Ma, L.H. Fu, L. Yang, Y.C. Zhou, C. Lu, Finite element simulations on erosion and crack propagation in thermal barrier coatings, High Temp. Mater. Proc. 34 (2015) 387-393.
45. B.D. Beake, J. Roberts, L. Isern, C. Chalk, J.R. Nicholls, Elevated temperature micro-scale impact testing of thermal barrier coatings for erosion simulation, ICMCTF 2024, San Diego, USA.

Figure Captions

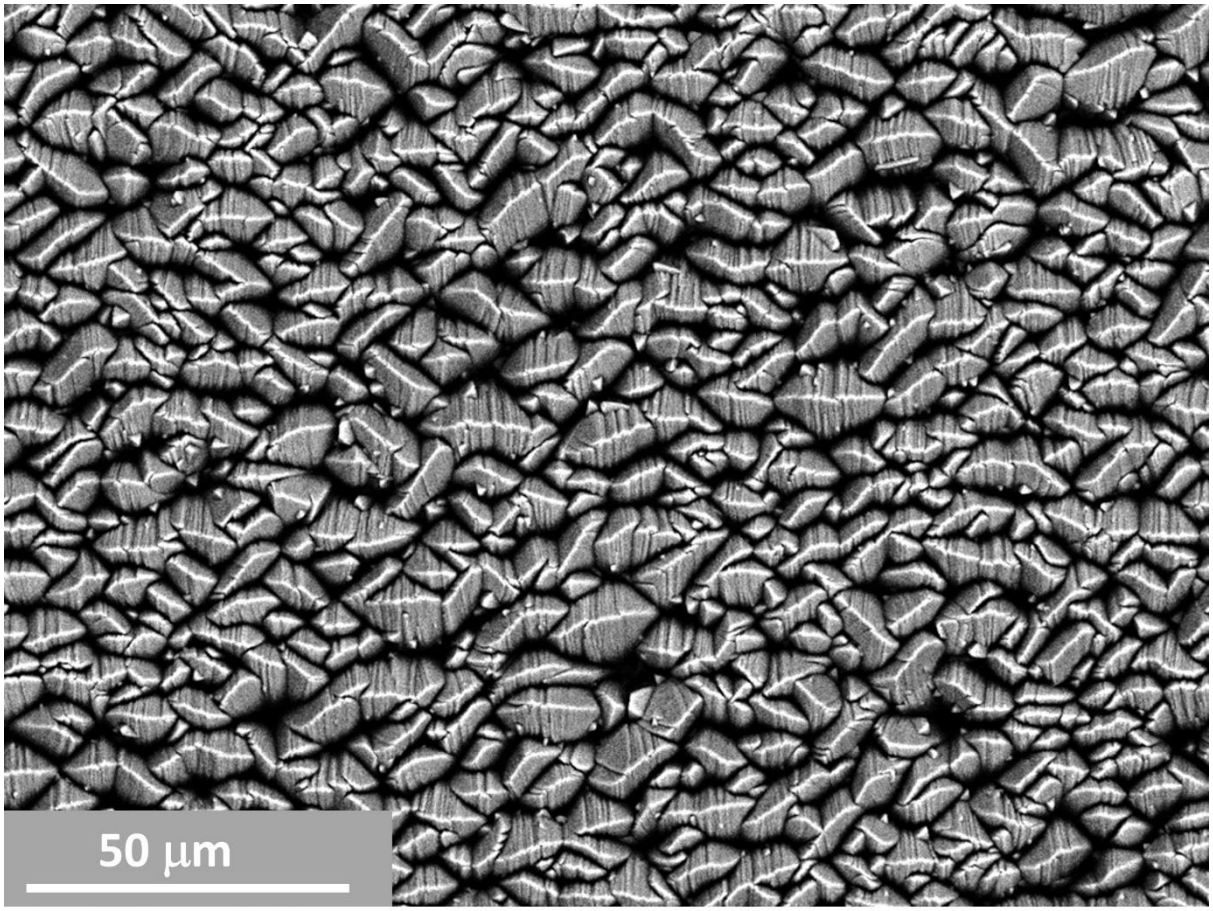
1. SEM images of top and side views of 7YSZ (a-c) and GZO (d-f) coatings.
2. Gaussian and rectangular distributions.
3. Typical depth and velocity vs. time data for a single impact.
4. Nano-impact. Typical impact depth vs. number of impacts curves at 5-50 mN (a) 7YSZ (b) GZO. Load dependence of (c) initial impact depth and (d) final impact depth.
5. Micro-impact. Typical impact depth vs. number of impacts curves at 500-3000 mN (a) 7YSZ (b) GZO. Load dependence of (c) initial impact depth and (d) final impact depth.
6. SEM images of 90° micro-impact craters (a) 500 mN 7YSZ; (b) 2000 mN 7YSZ; (c,d) 500 mN on GZO.
7. SEM images of FIB-milled sections through cyclic impact craters on 7YSZ at (a,b) 500 mN (c,d) 3000 mN.

8. Angle dependence of typical 500 and 1500 mN impact depth curves on (a) 7YSZ (b) GZO. (c) Comparative final impact depth data on both TBCs at 75° and 90°. SEM images at 1500 mN (e) 7YSZ at 90°, (f) 7YSZ at 75°, (g) GZO at 90°, (h) GZO at 75°.
9. Laser scanning confocal images of randomised impact tests at 500 mN. (a) 7YSZ, Gaussian distribution (b) 7YSZ, rectangular distribution (c) GZO, Gaussian distribution (d) GZO, rectangular distribution, (e,f) tests in (c,d) overlaid with impact distributions.
10. Laser scanning confocal images of randomised impact tests at 1000 mN (a and b) repeat tests with the same rectangular distribution. (c) Gaussian distribution (d) BSE SEM image of the Gaussian test, with higher resolution BSE SEM image from the dashed region shown in (e).
11. Influence of distribution type on variation in final depth with number of impacts for GZO at (a) 500 mN (b) 1000 mN. (c) KE absorbed in Gaussian tests on GZO.
12. Mass loss in erosion tests with (a) angular and (b) spherical alumina particles. Two tests were performed for each set of conditions (R in the figure legends signify the repeat tests).
13. SEM images of cross-sections of 7YSZ eroded by (a) spherical and (b) angular alumina particles. GZO cross-section (c) in a 500 mN randomly spatially distributed micro-impact test and (d) eroded by angular alumina particles.
14. SEM images of the top-surface of eroded TBCs (a) GZO (b,c) 7YSZ at the edge of the eroded region.
15. Load dependence of (a) initial and (b) final impact volume in cyclic impact tests.

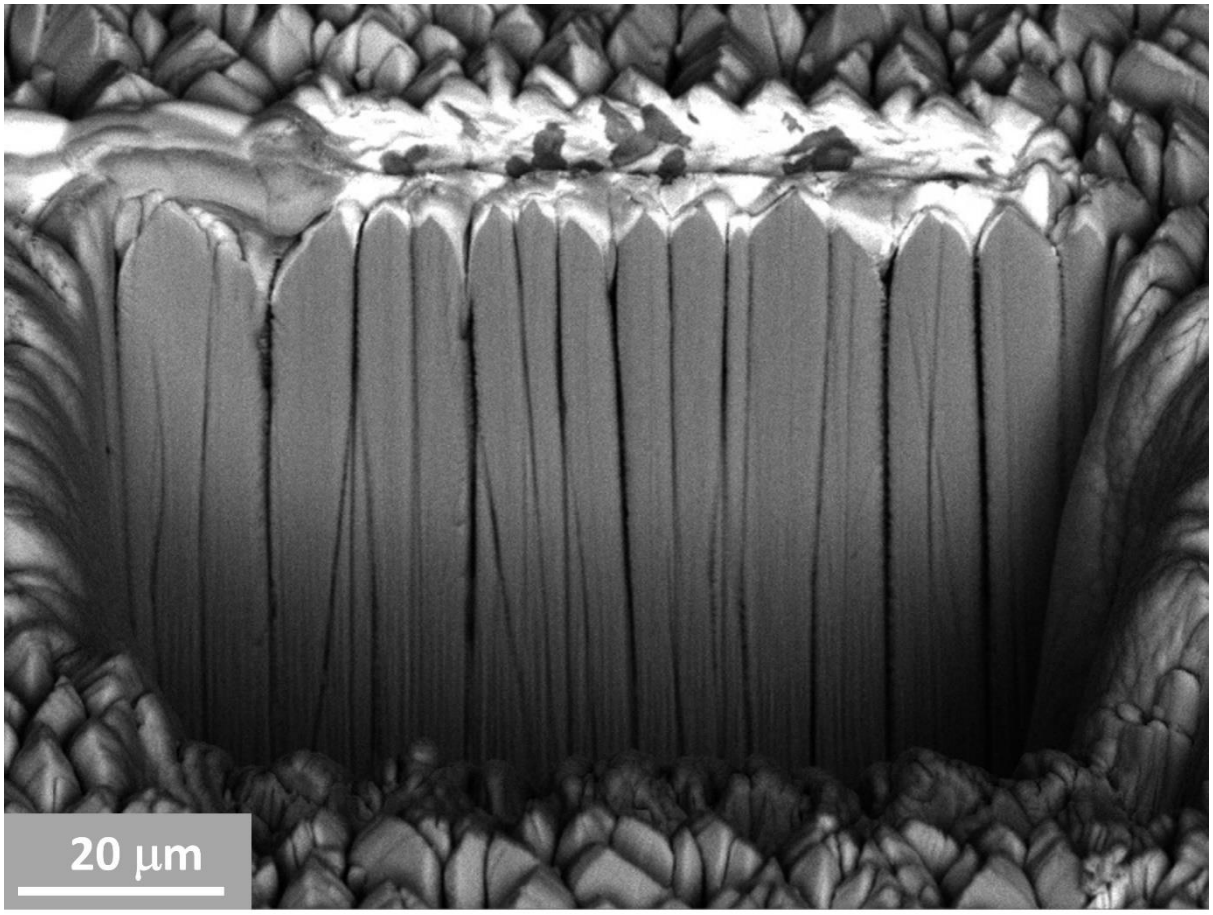
Figures



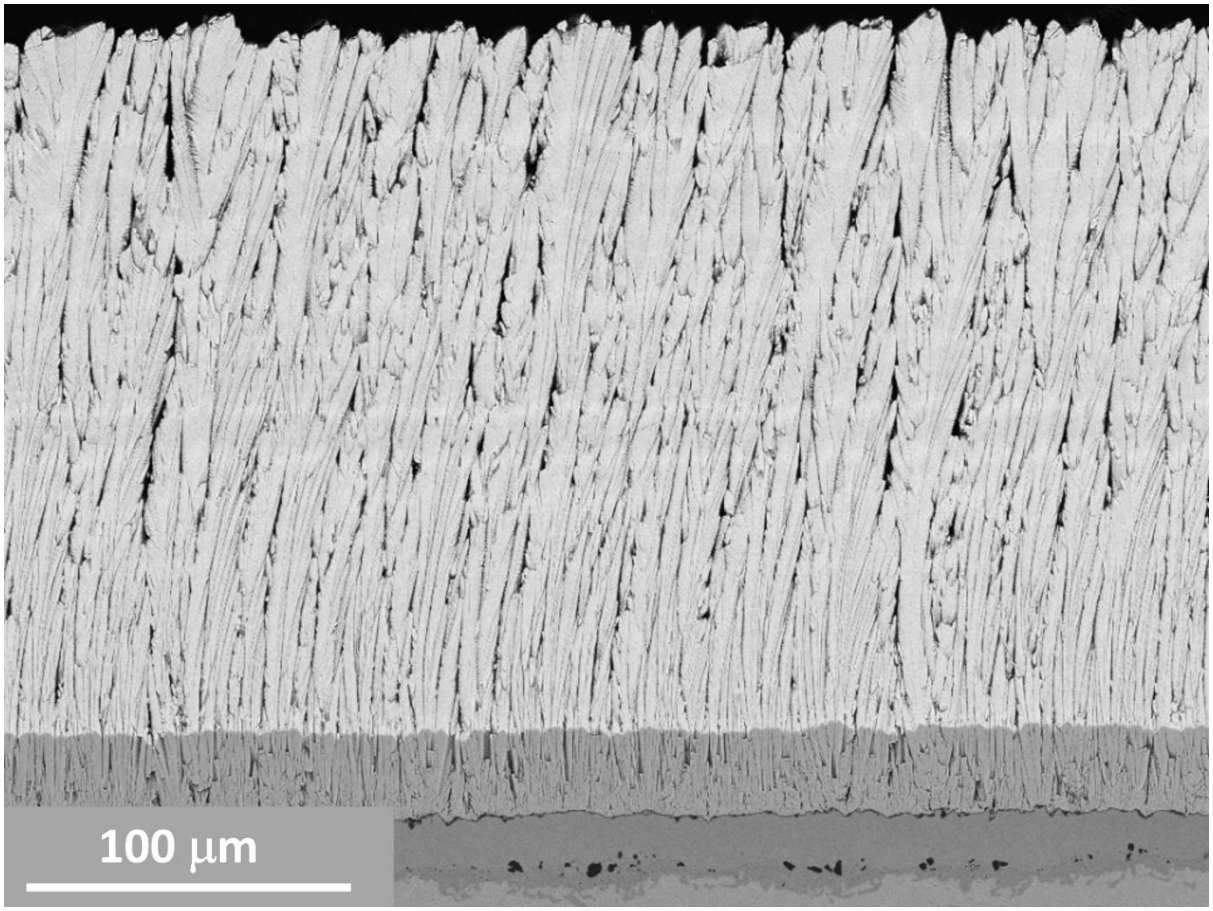
1(a)



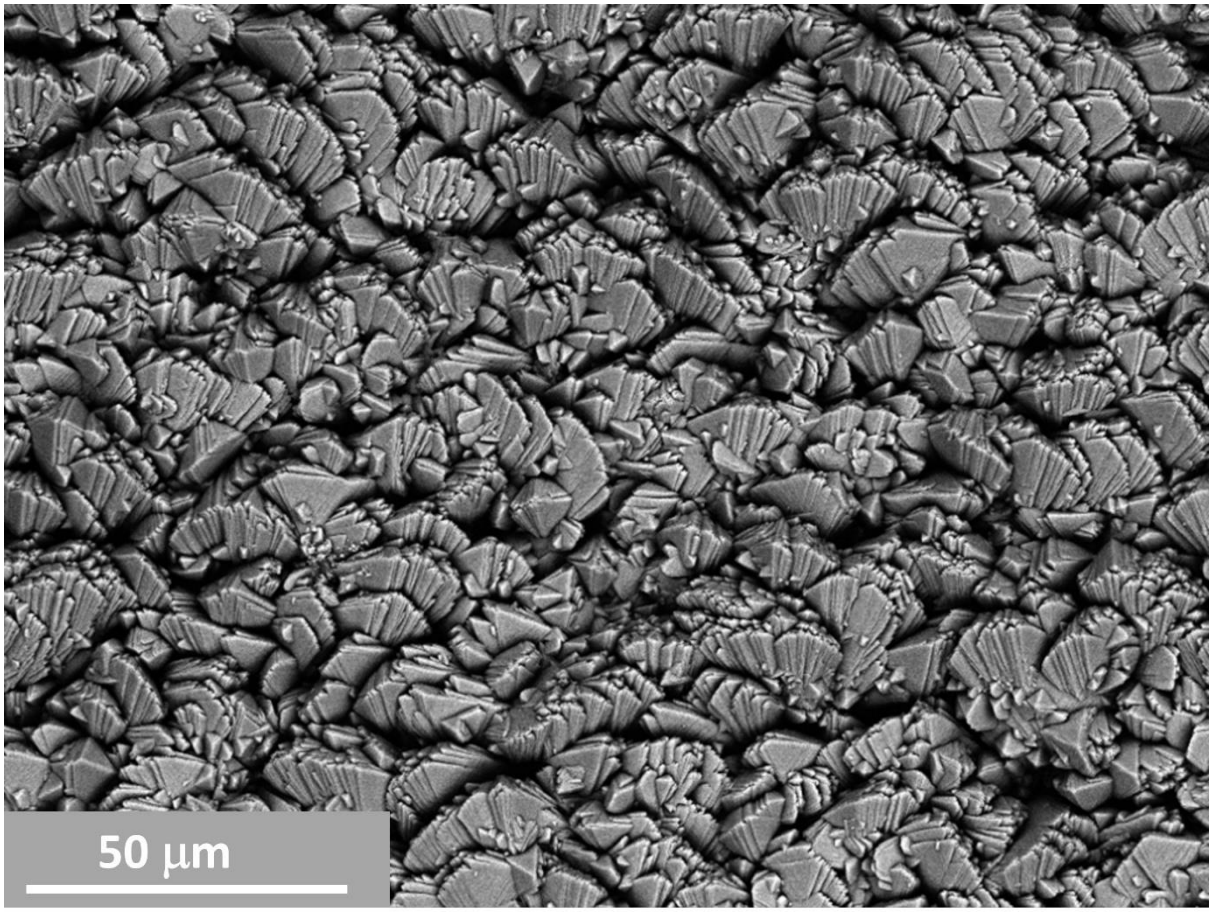
1(b)



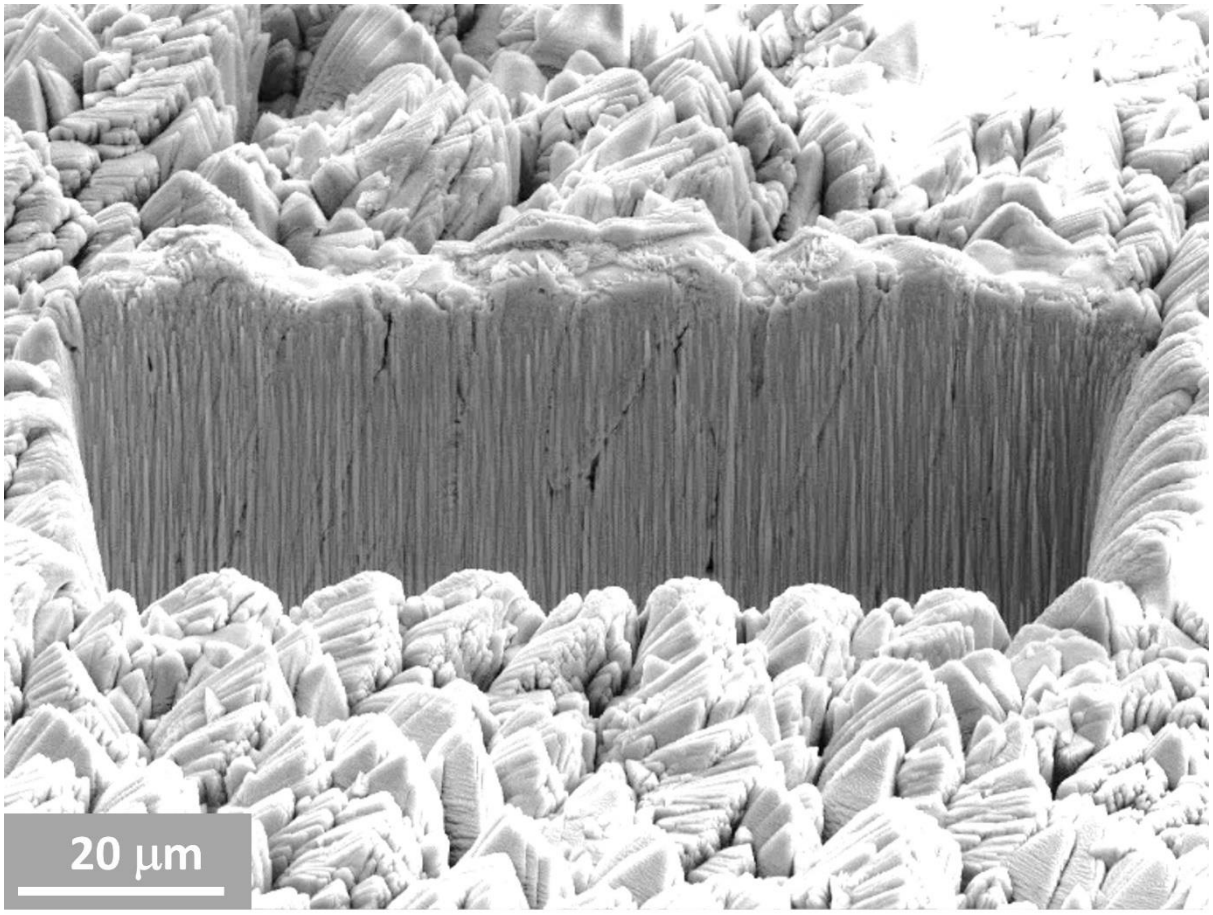
1(c)



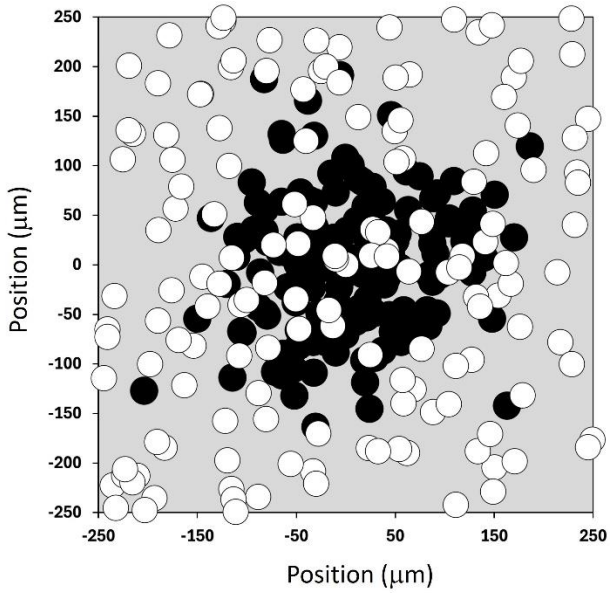
1(d)



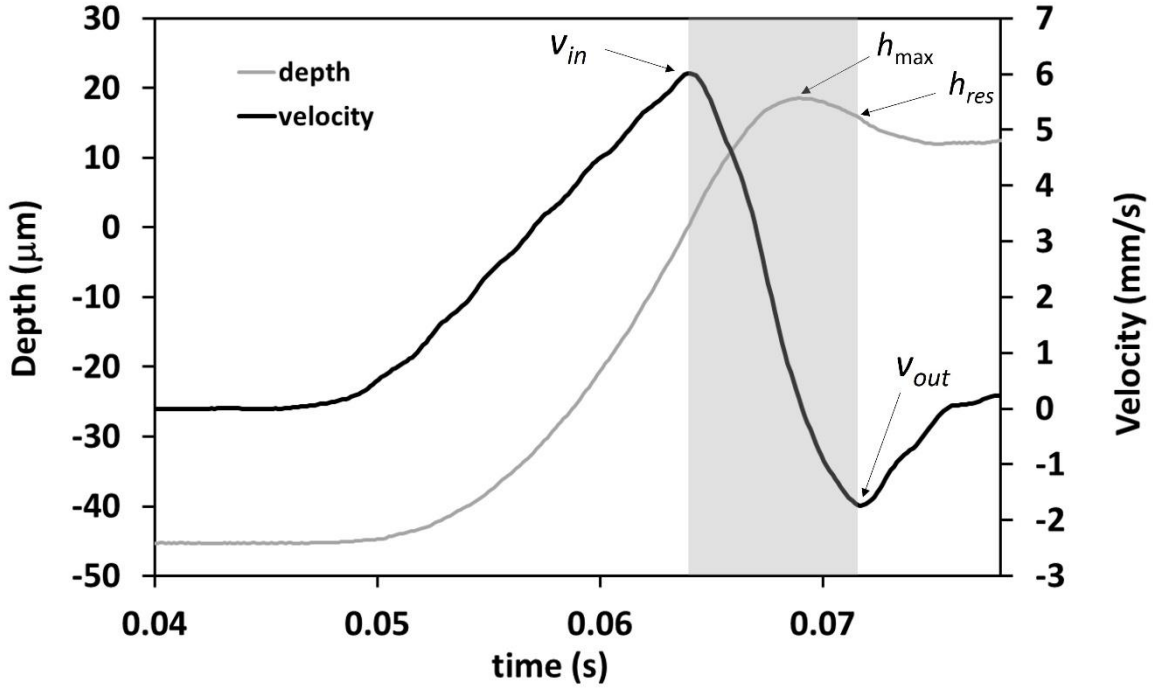
1(e)


20 μm

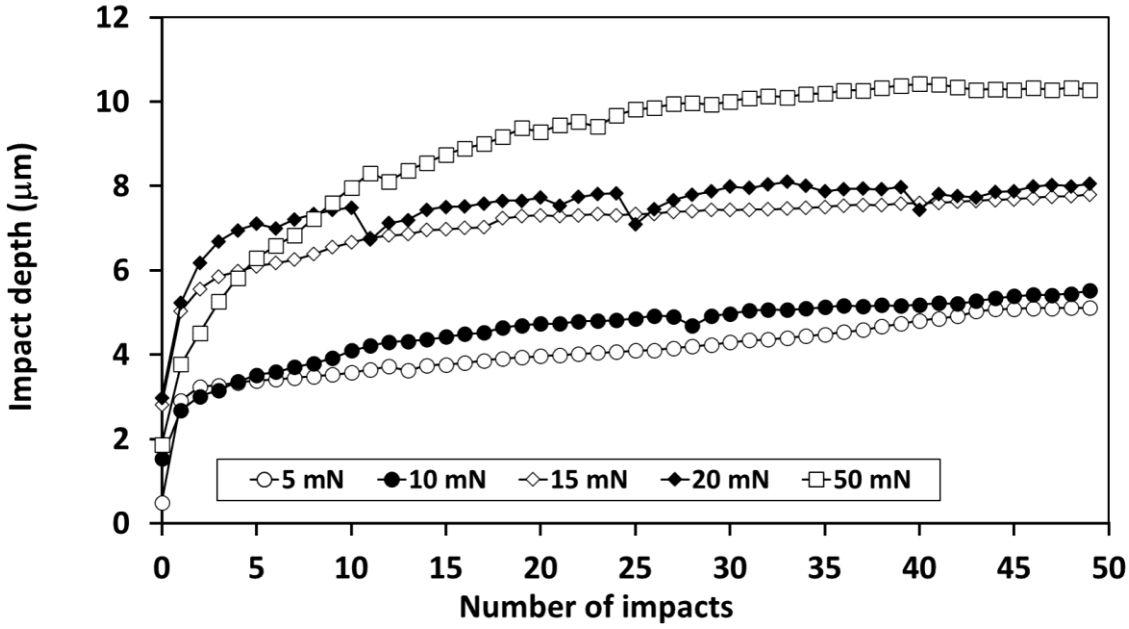
1(f)


250
200
150
100
50
0
-50
-100
-150
-200
-250
Position (μm)
-250
-150
-50
50
150
250
Position (μm)

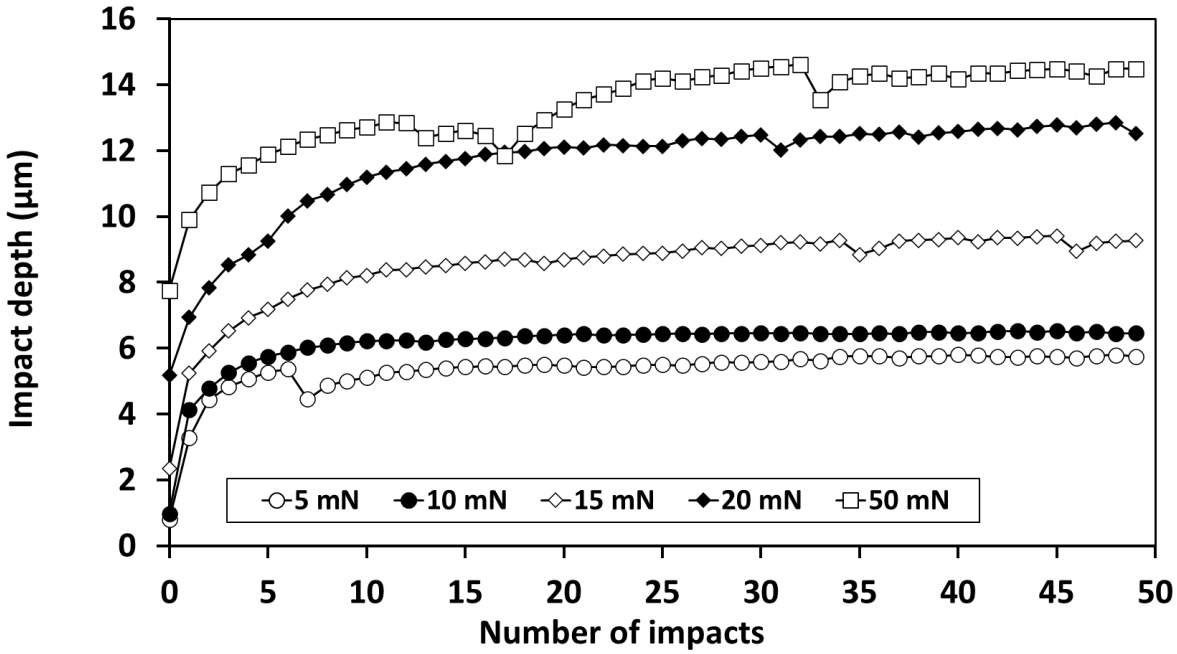
2.


depth
velocity
v_{in}
h_{max}
h_{res}
v_{out}
Depth (μm)
Velocity (mm/s)
time (s)
30
20
10
0
-10
-20
-30
-40
-50
7
6
5
4
3
2
1
0
-1
-2
-3
0.04
0.05
0.06
0.07

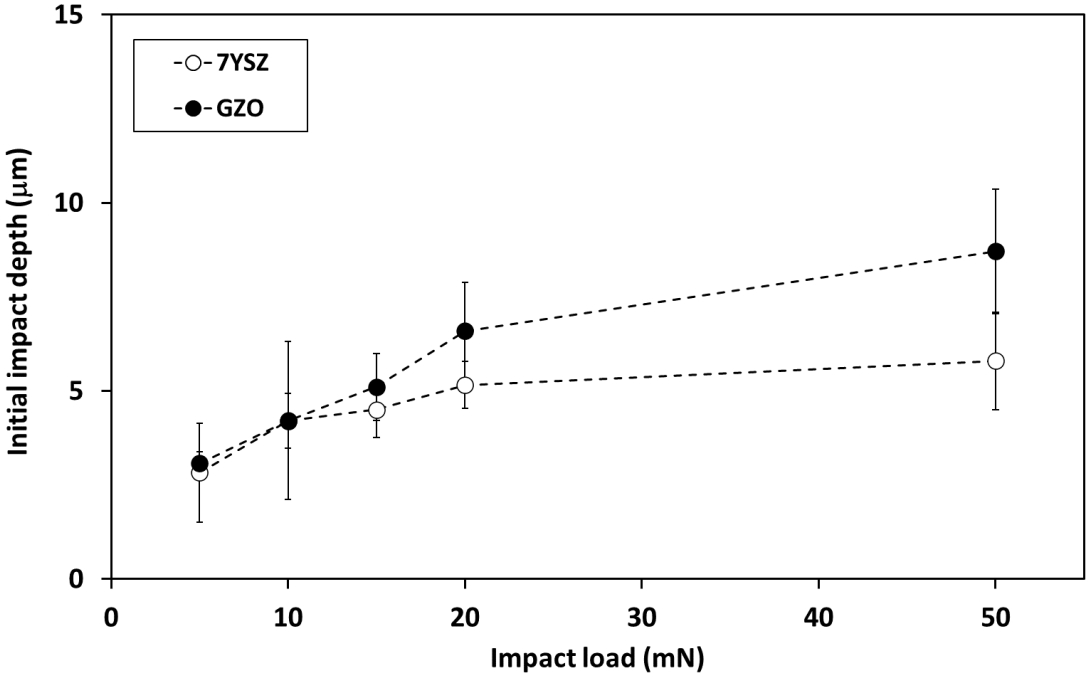
3.


Impact depth (μm)
Number of impacts
5 mN
10 mN
15 mN
20 mN
50 mN
12
10
8
6
4
2
0
0
5
10
15
20
25
30
35
40
45
50

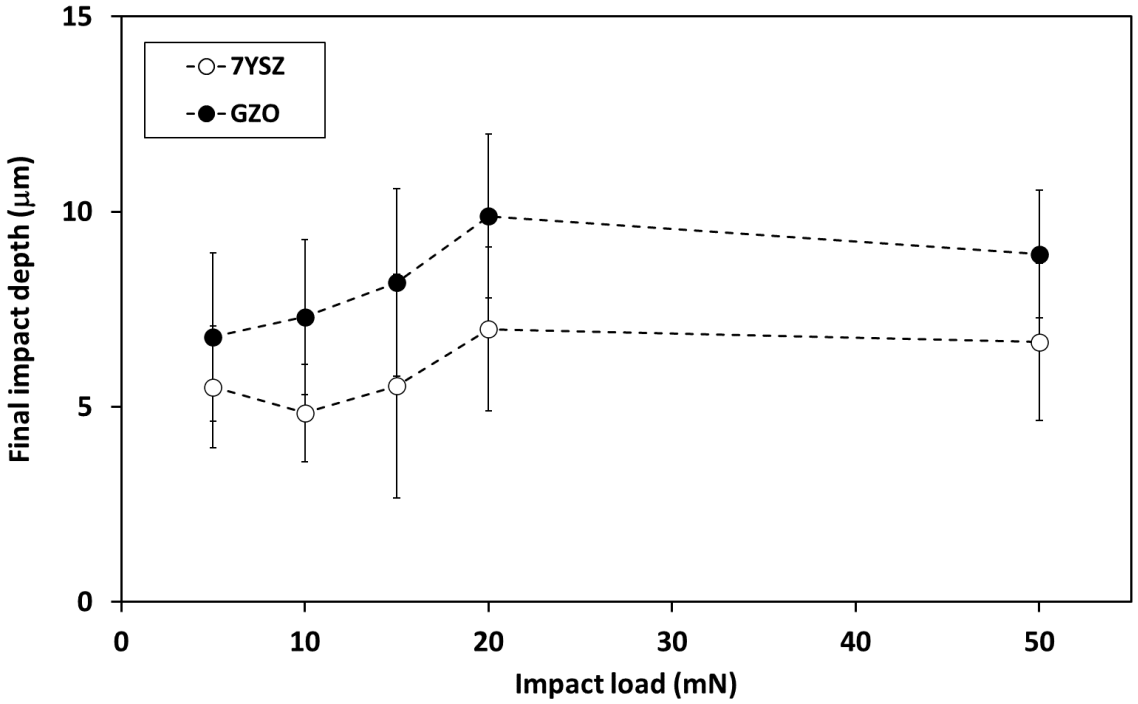
4(a).


Impact depth (μm)
Number of impacts
5 mN
10 mN
15 mN
20 mN
50 mN

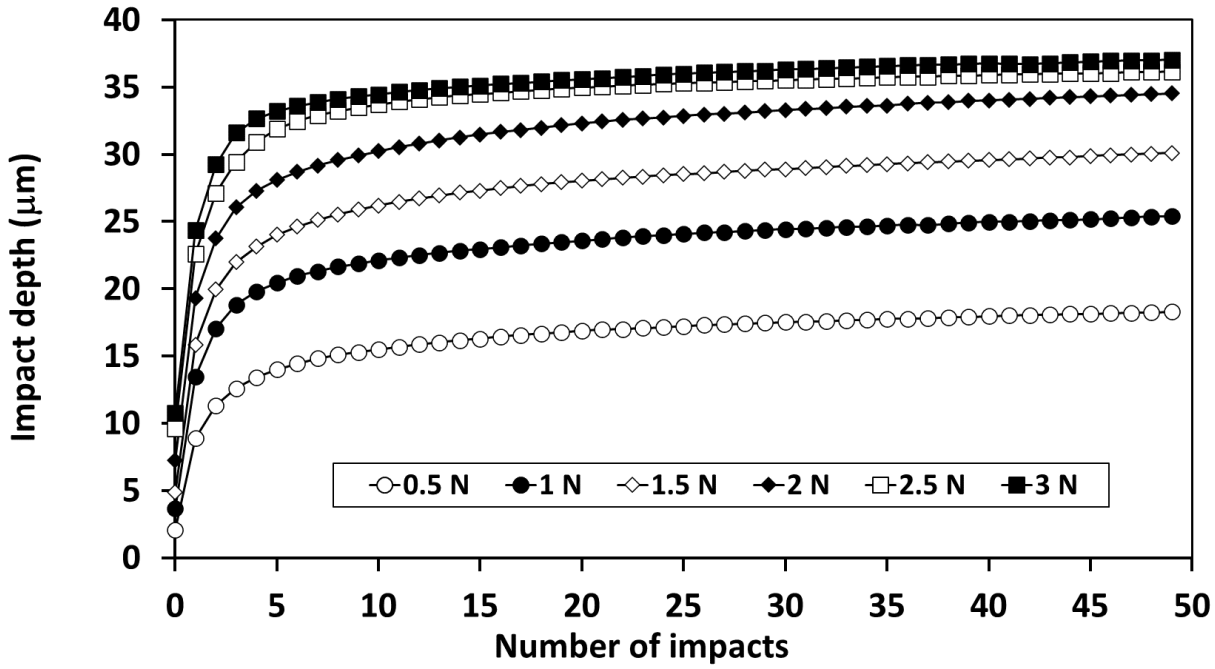
4(b).


Initial impact depth (μm)
Impact load (mN)
7YSZ
GZO

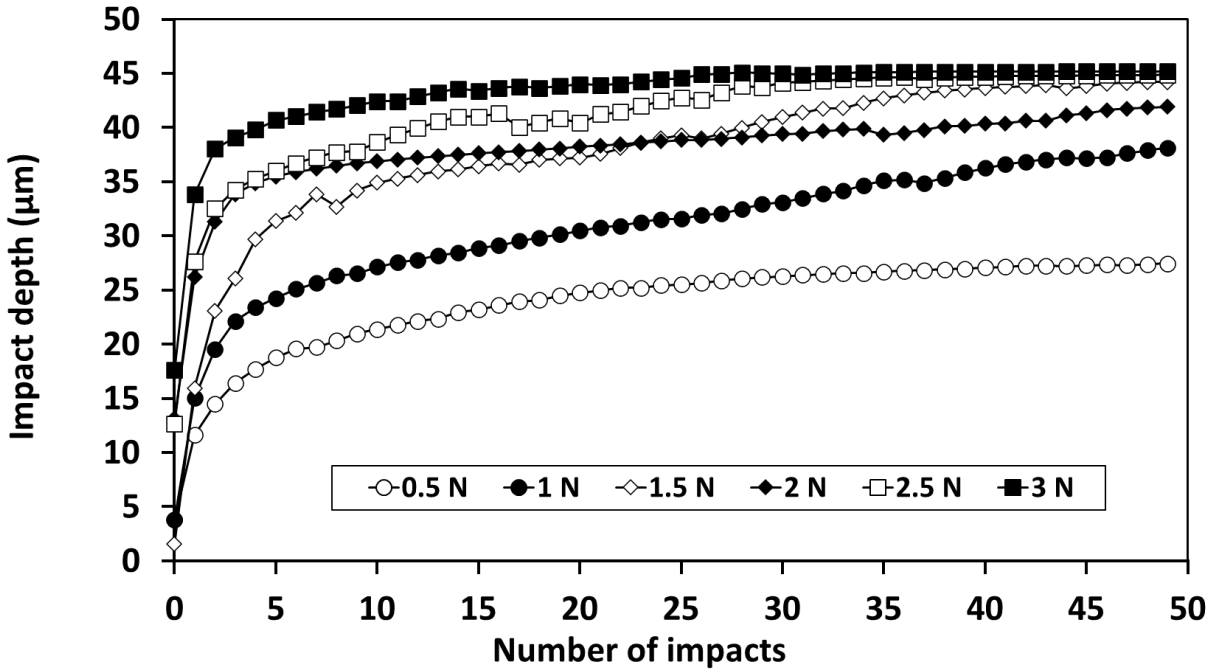
4(c).


7YSZ
GZO
Final impact depth (μm)
Impact load (mN)
0
5
10
15
0
10
20
30
40
50

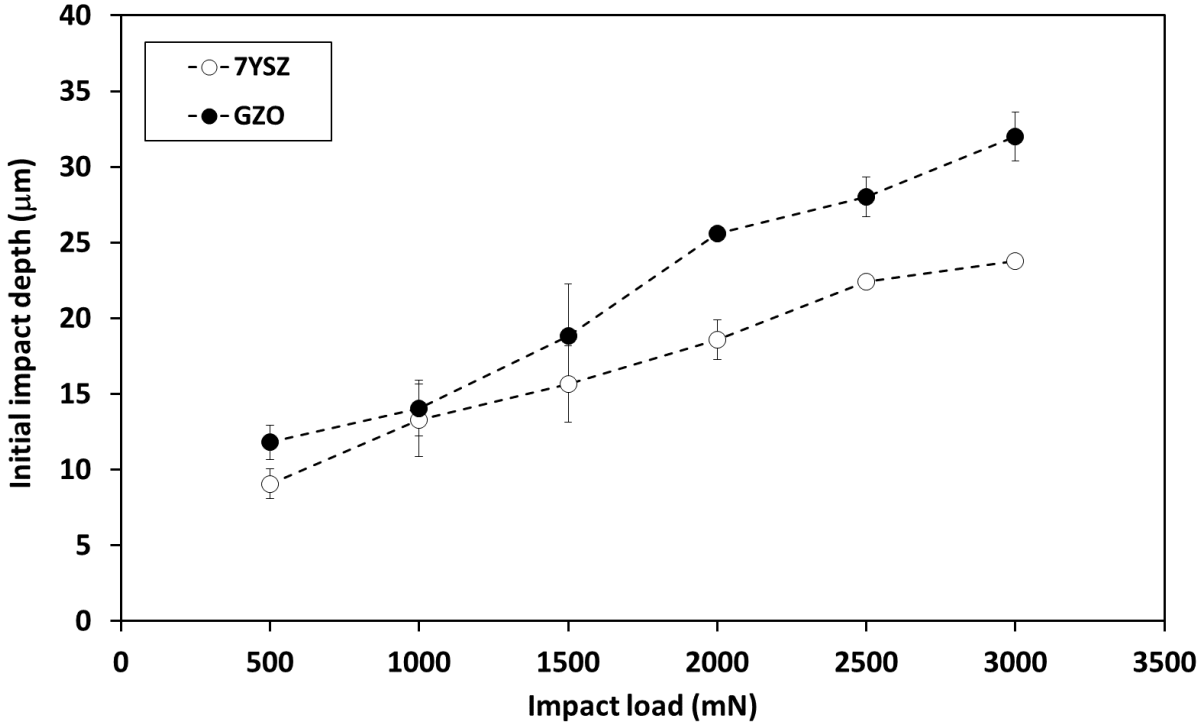
4(d).


0.5 N
1 N
1.5 N
2 N
2.5 N
3 N
Impact depth (μm)
Number of impacts
0
5
10
15
20
25
30
35
40
45
50

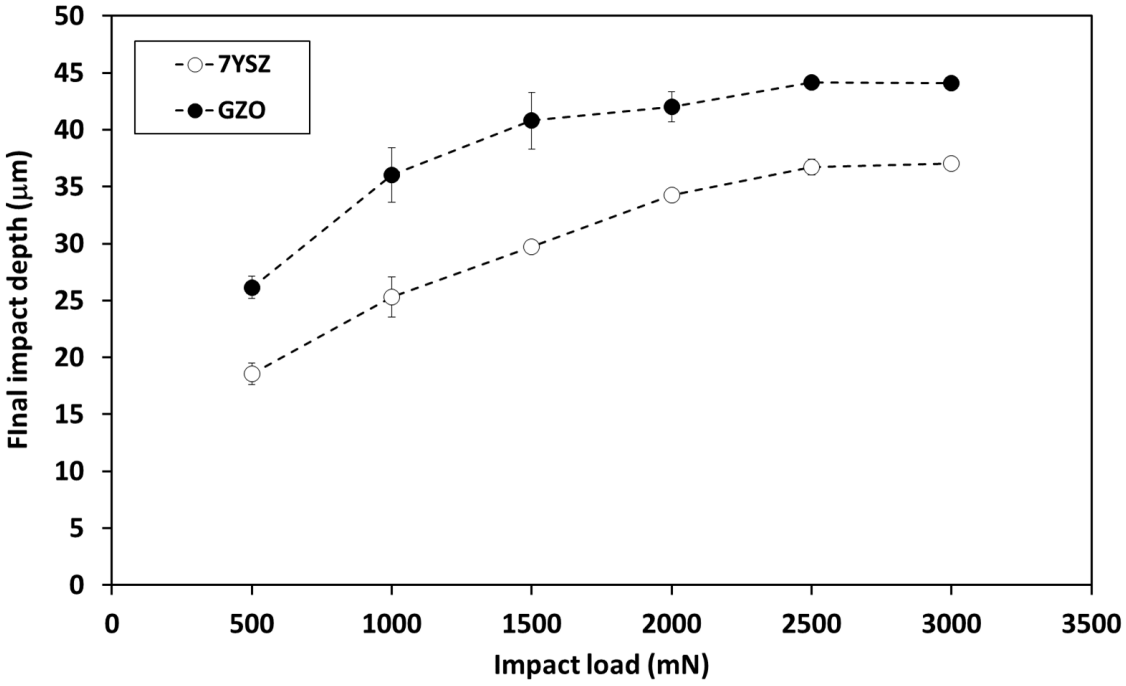
5(a).


Impact depth (μm)
Number of impacts
0.5 N
1 N
1.5 N
2 N
2.5 N
3 N

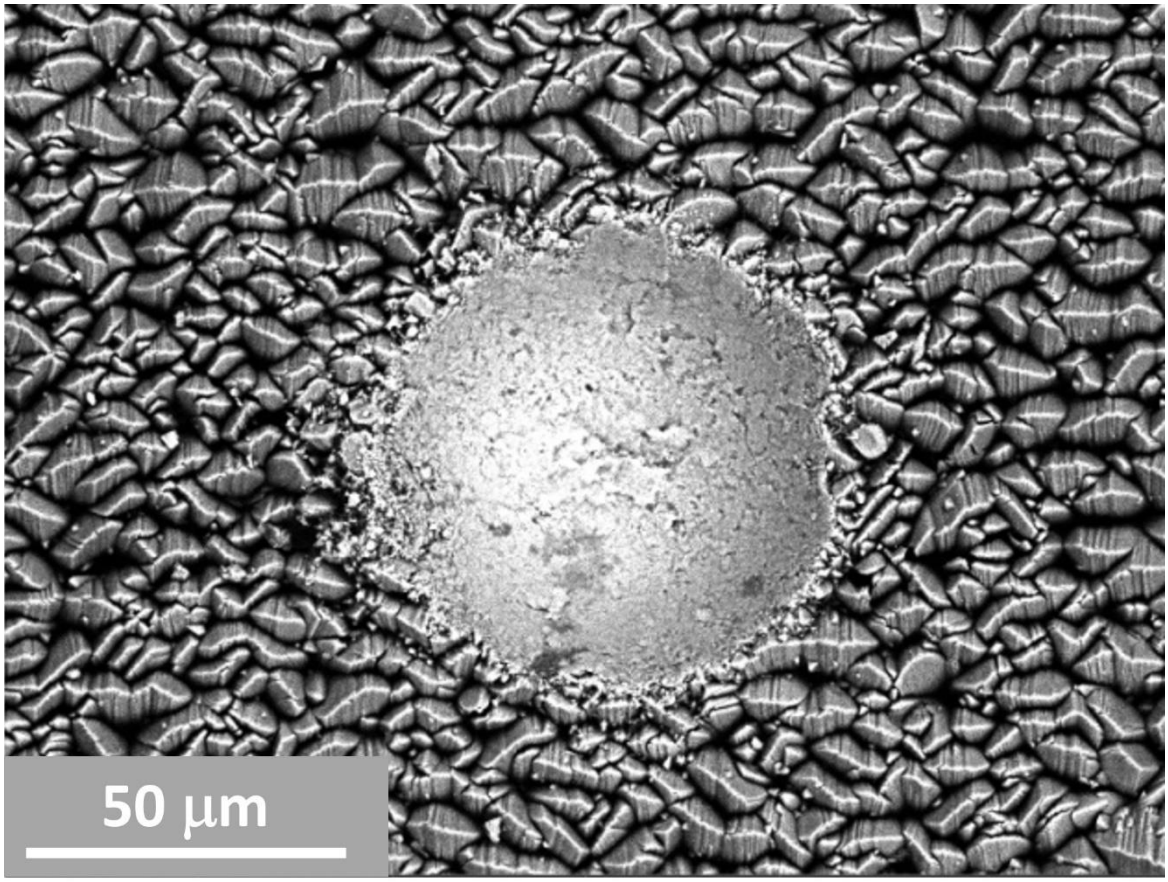
5(b).


Initial impact depth (μm)
Impact load (mN)
7YSZ
GZO

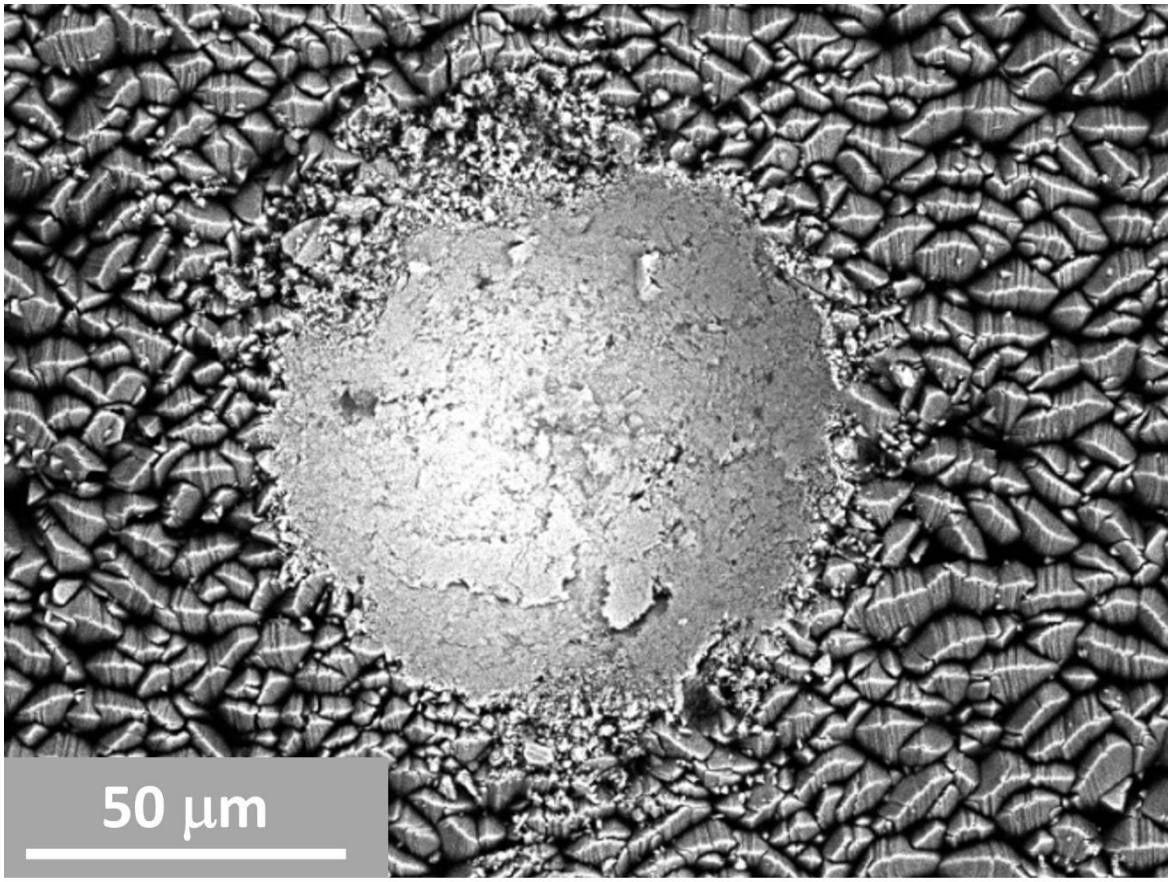
5(c).


7YSZ
GZO
Final impact depth (μm)
Impact load (mN)
0
5
10
15
20
25
30
35
40
45
50
0
500
1000
1500
2000
2500
3000
3500

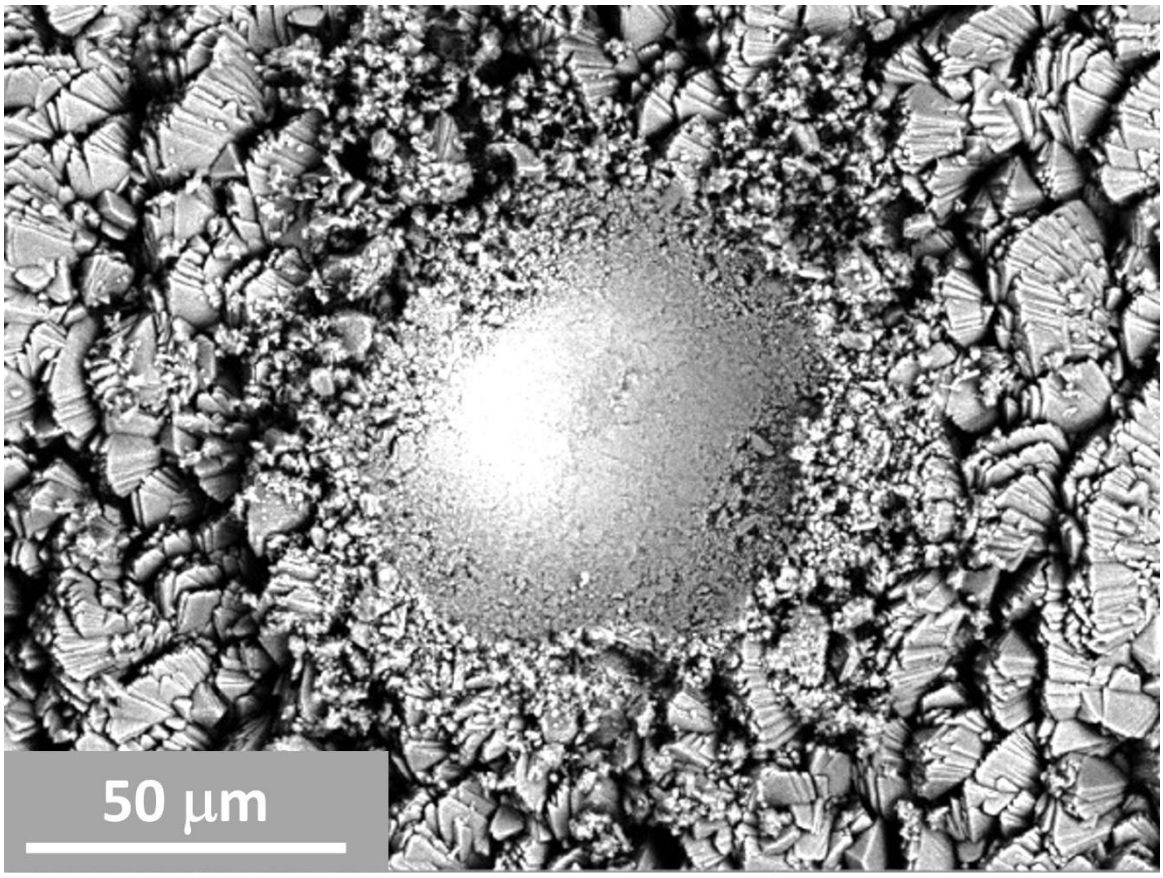
5(d).


50 μm

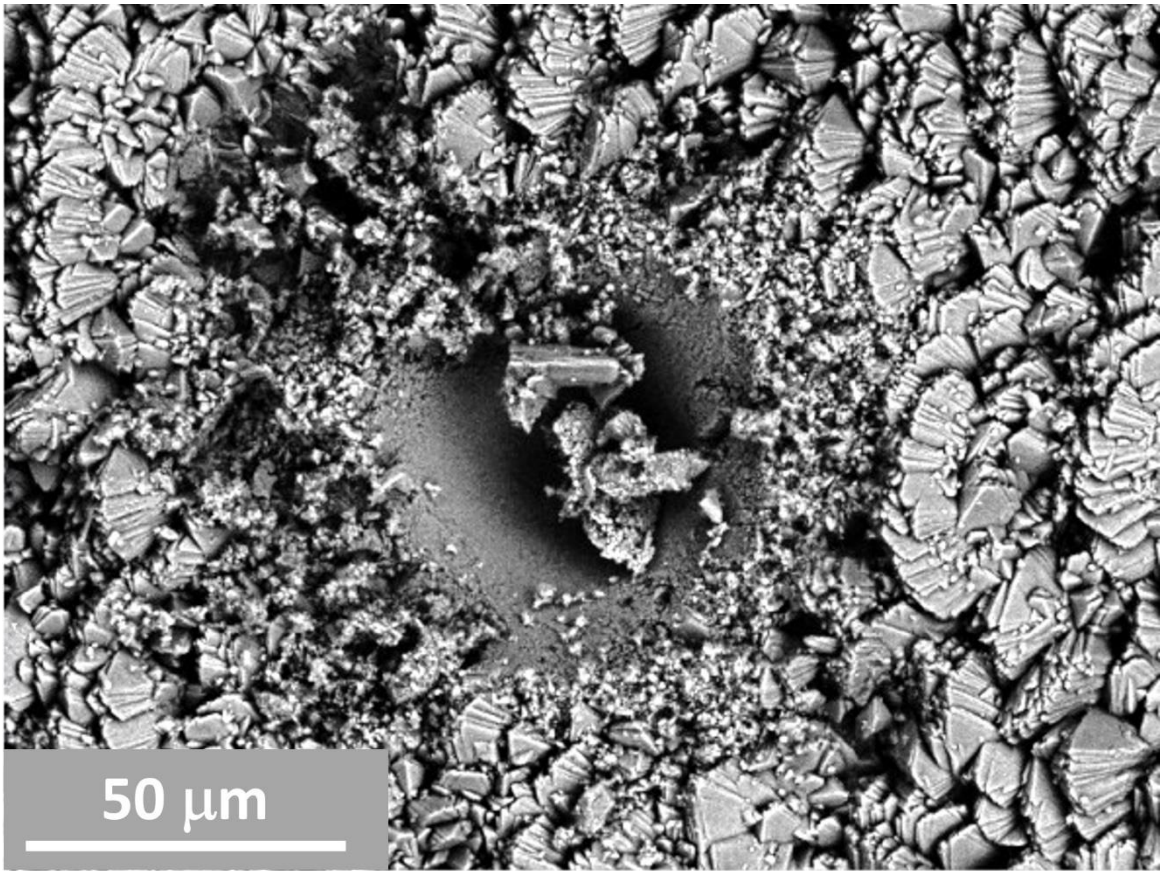
6(a)



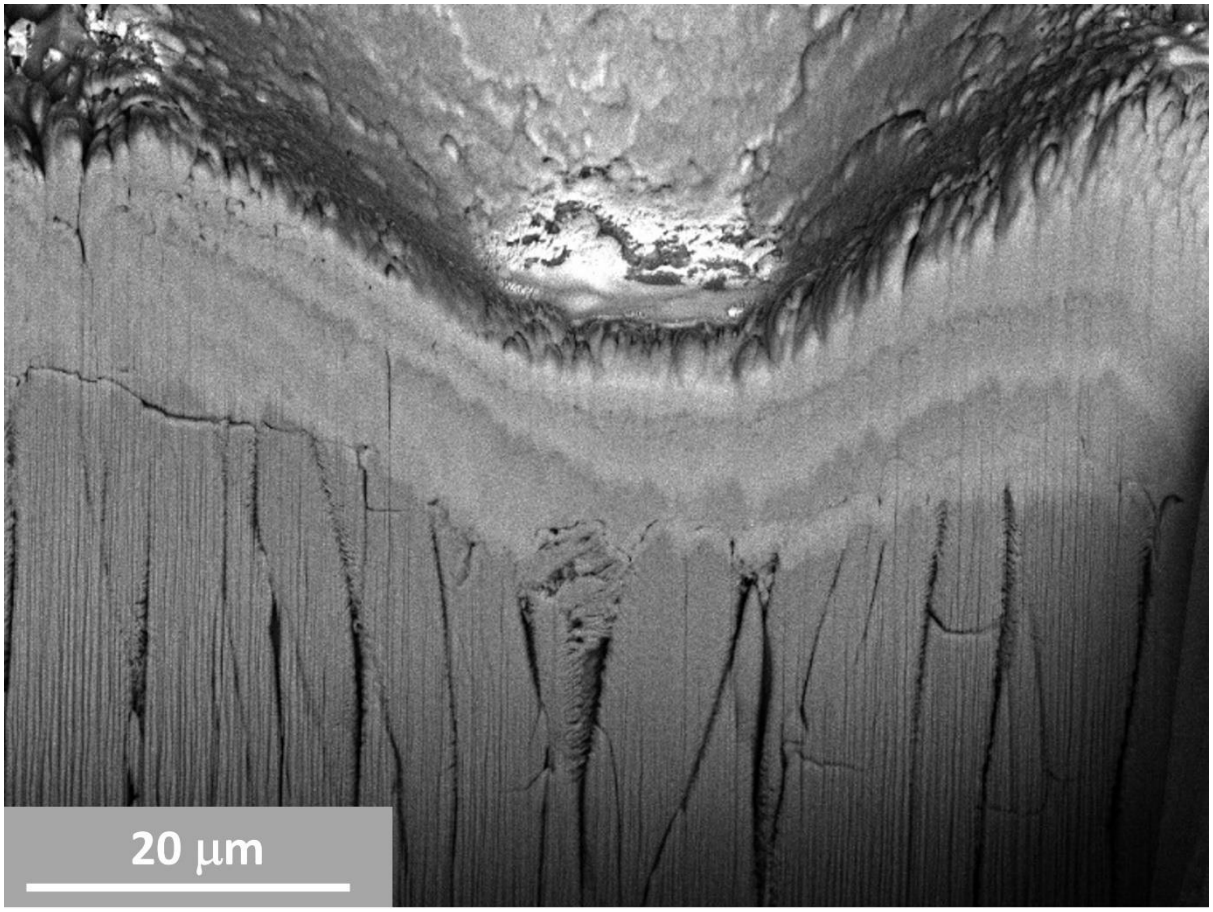
6(b)



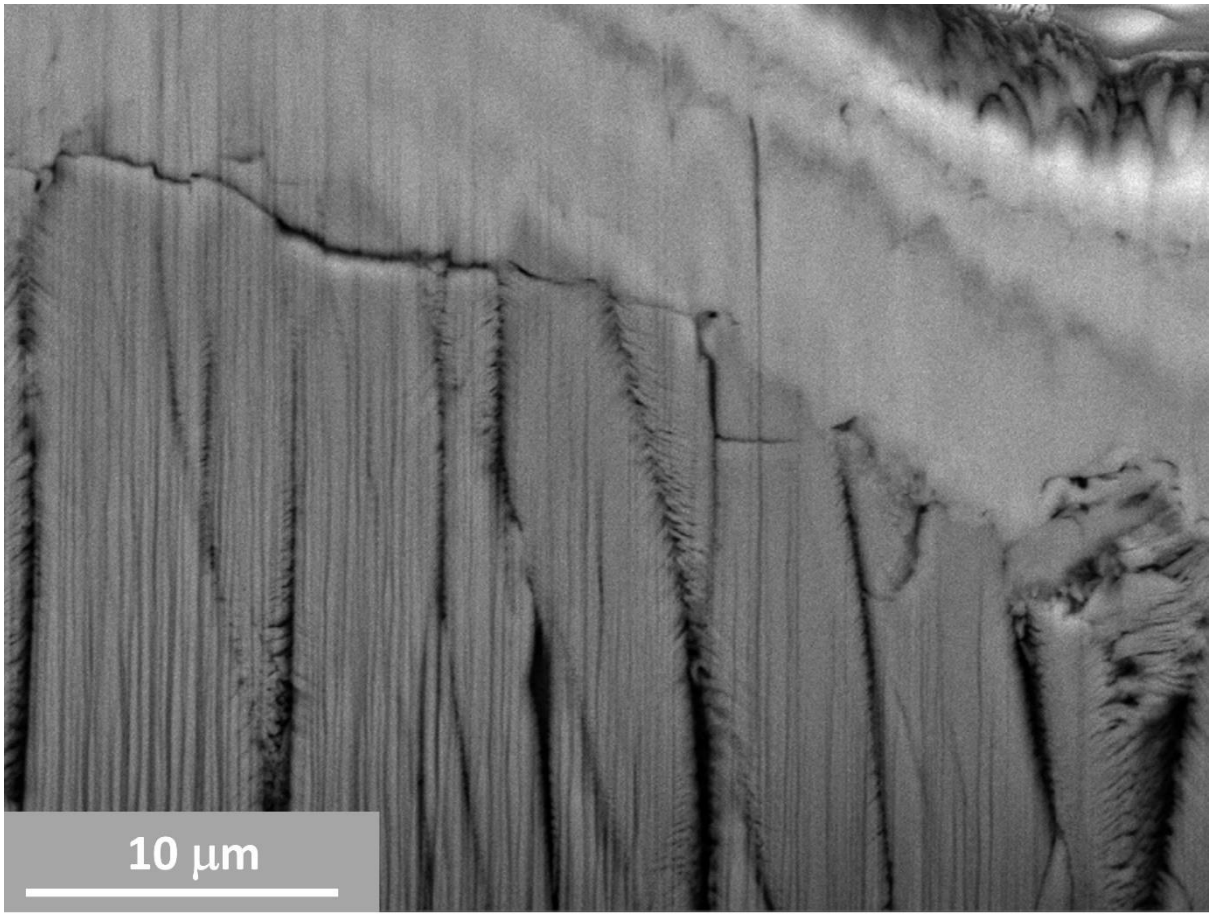
6(c)



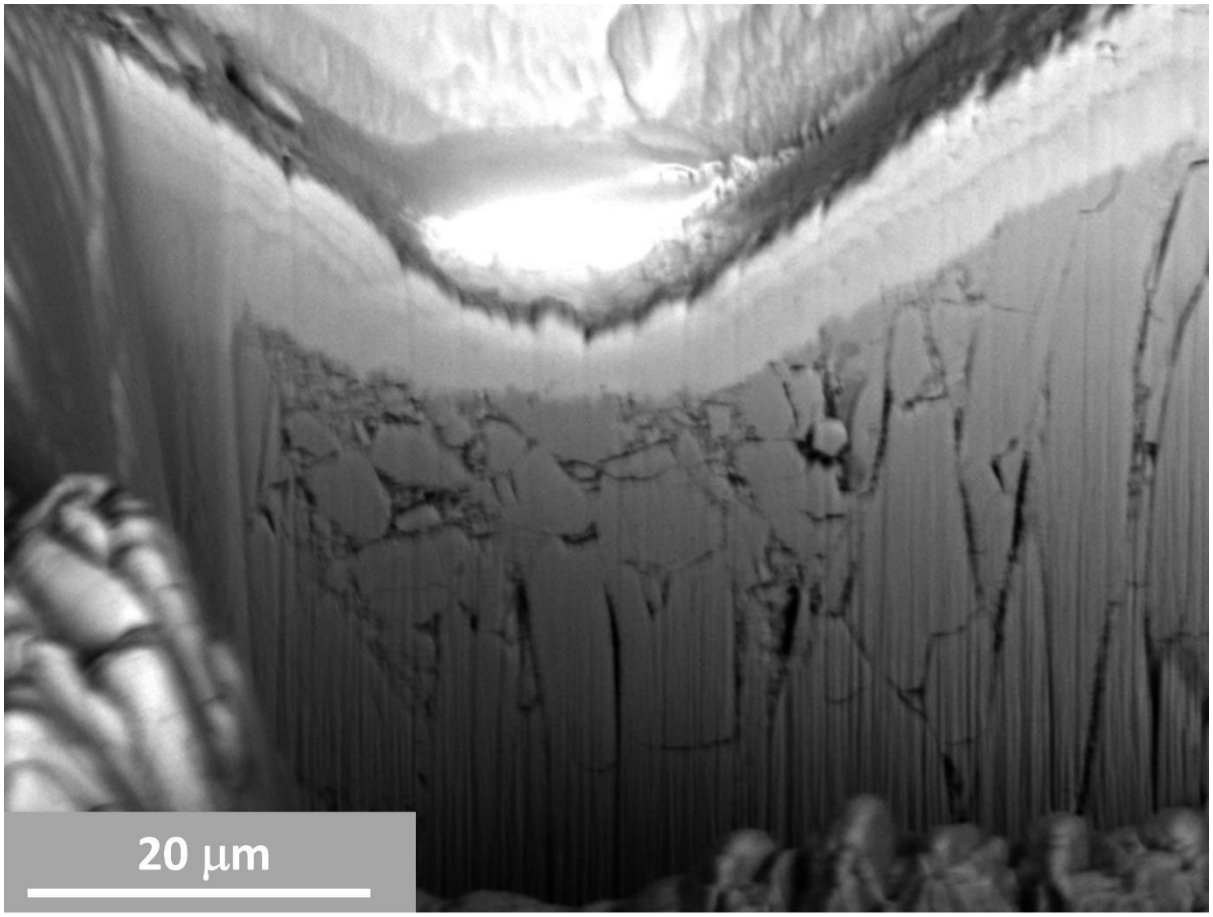
6(d)



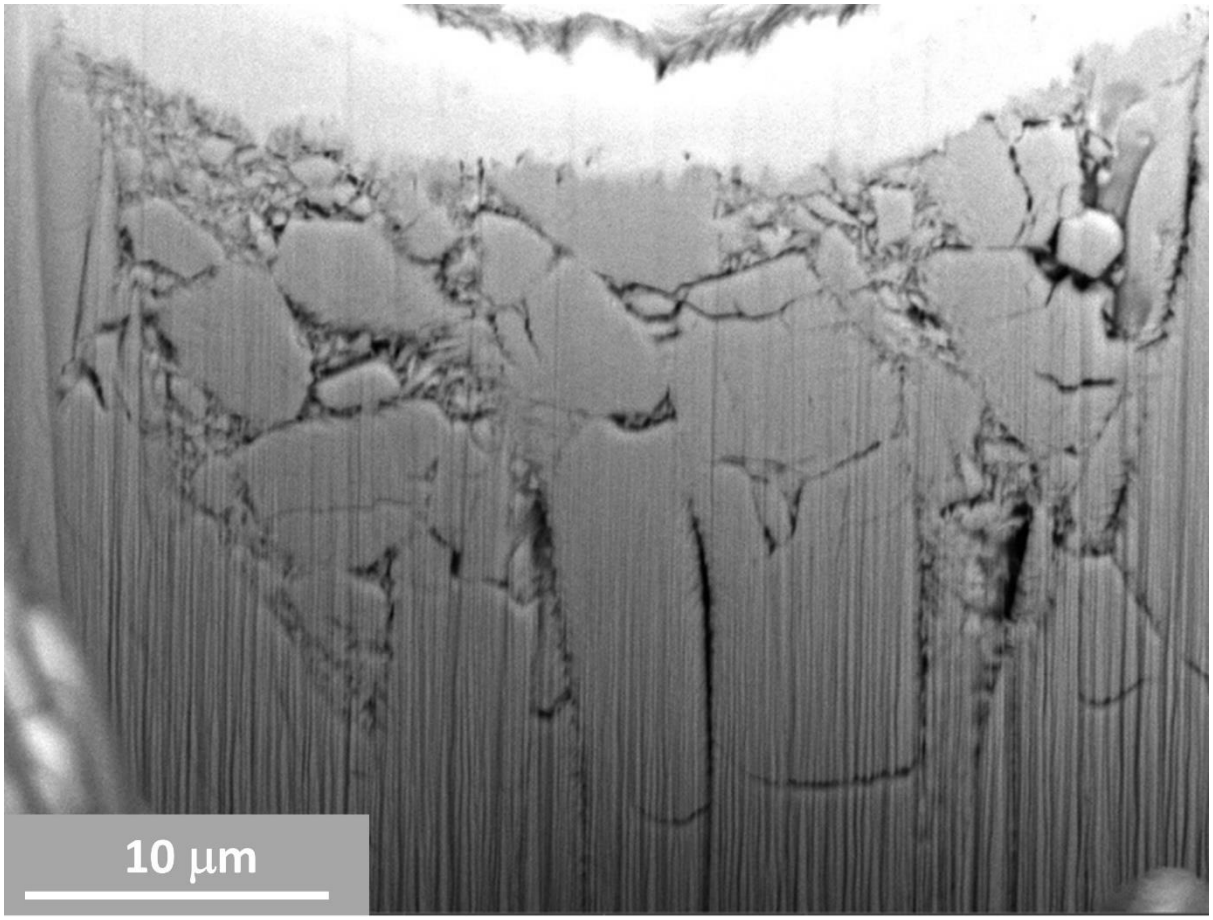
7(a)



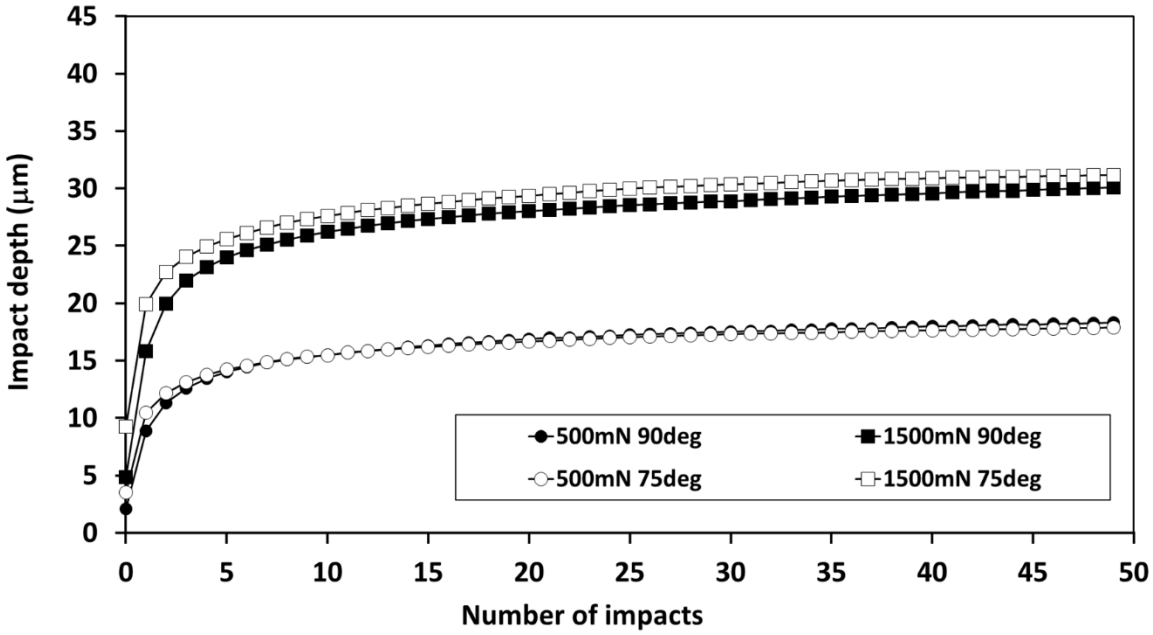
7(b)



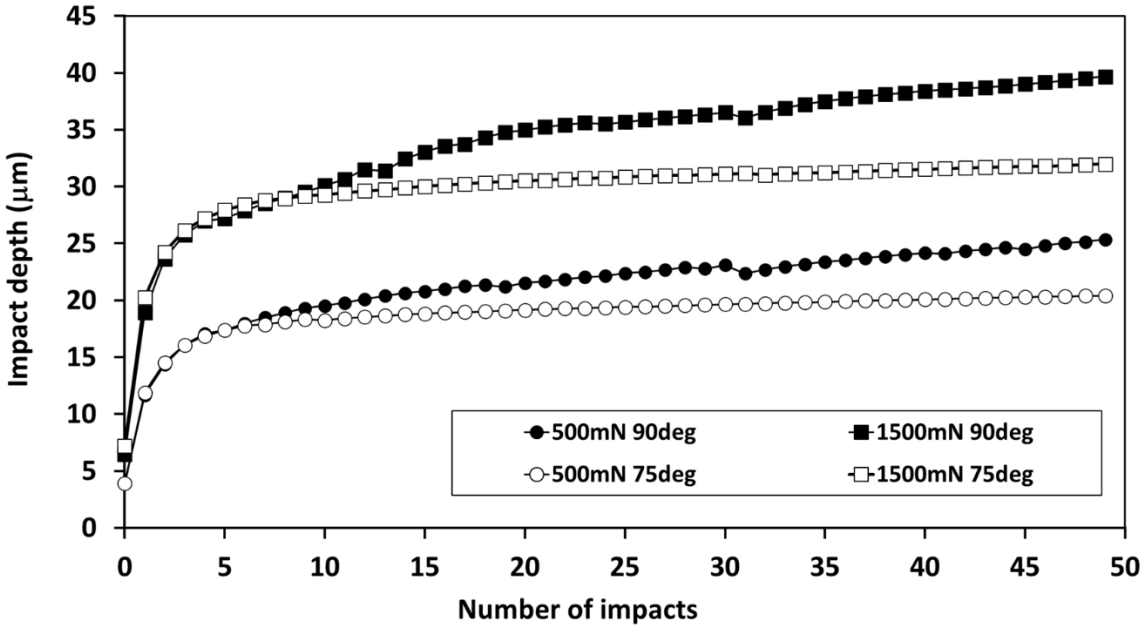
7(c)


10 μm

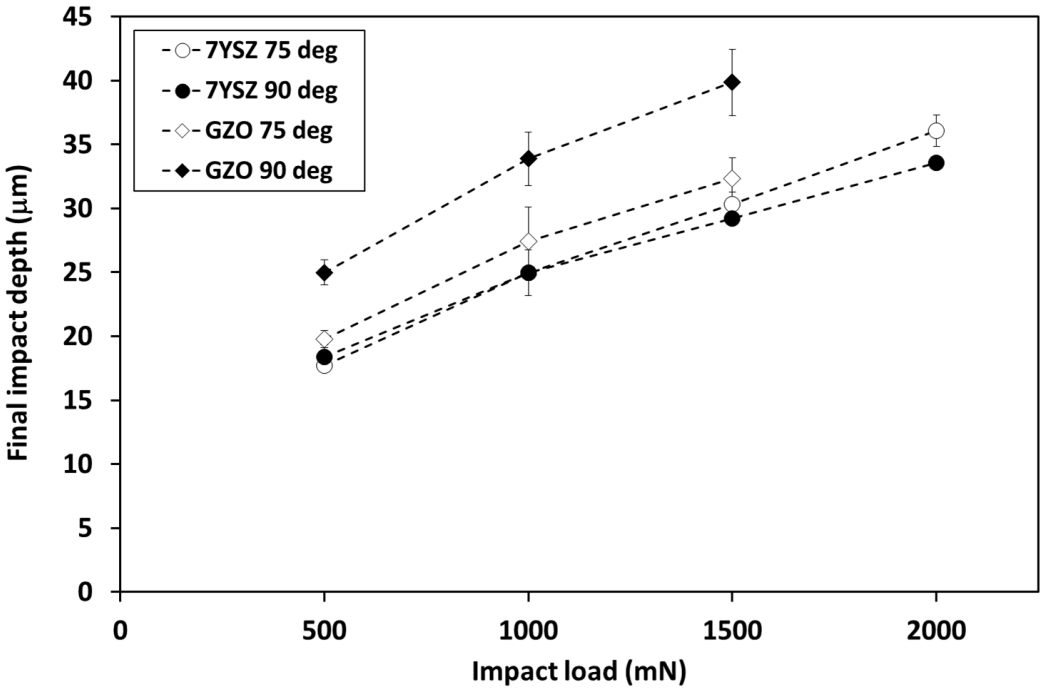
7(d)


Impact depth (μm)
Number of impacts
0
5
10
15
20
25
30
35
40
45
50
500mN 90deg
1500mN 90deg
500mN 75deg
1500mN 75deg

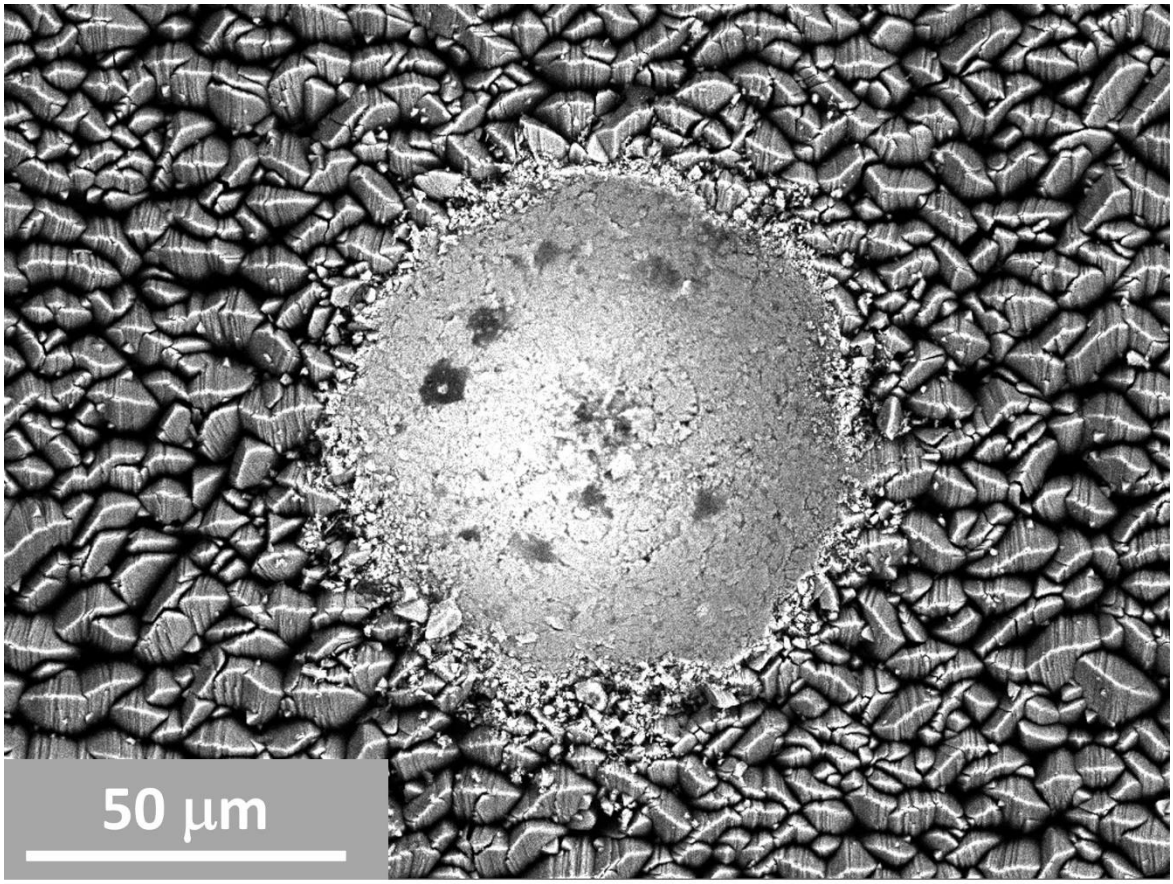
8(a).


Impact depth (µm)
Number of impacts
500mN 90deg
1500mN 90deg
500mN 75deg
1500mN 75deg

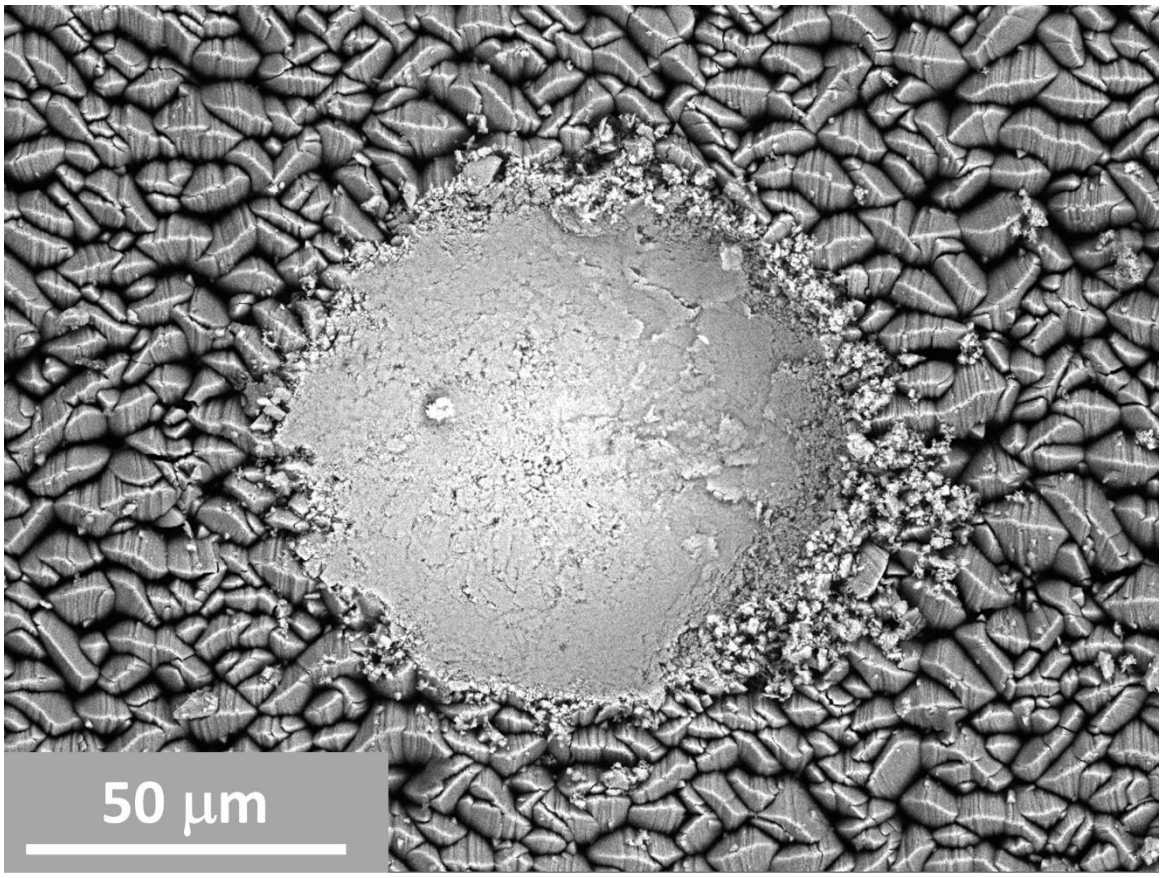
8(b).


Final impact depth (µm)
Impact load (mN)
7YSZ 75 deg
7YSZ 90 deg
GZO 75 deg
GZO 90 deg

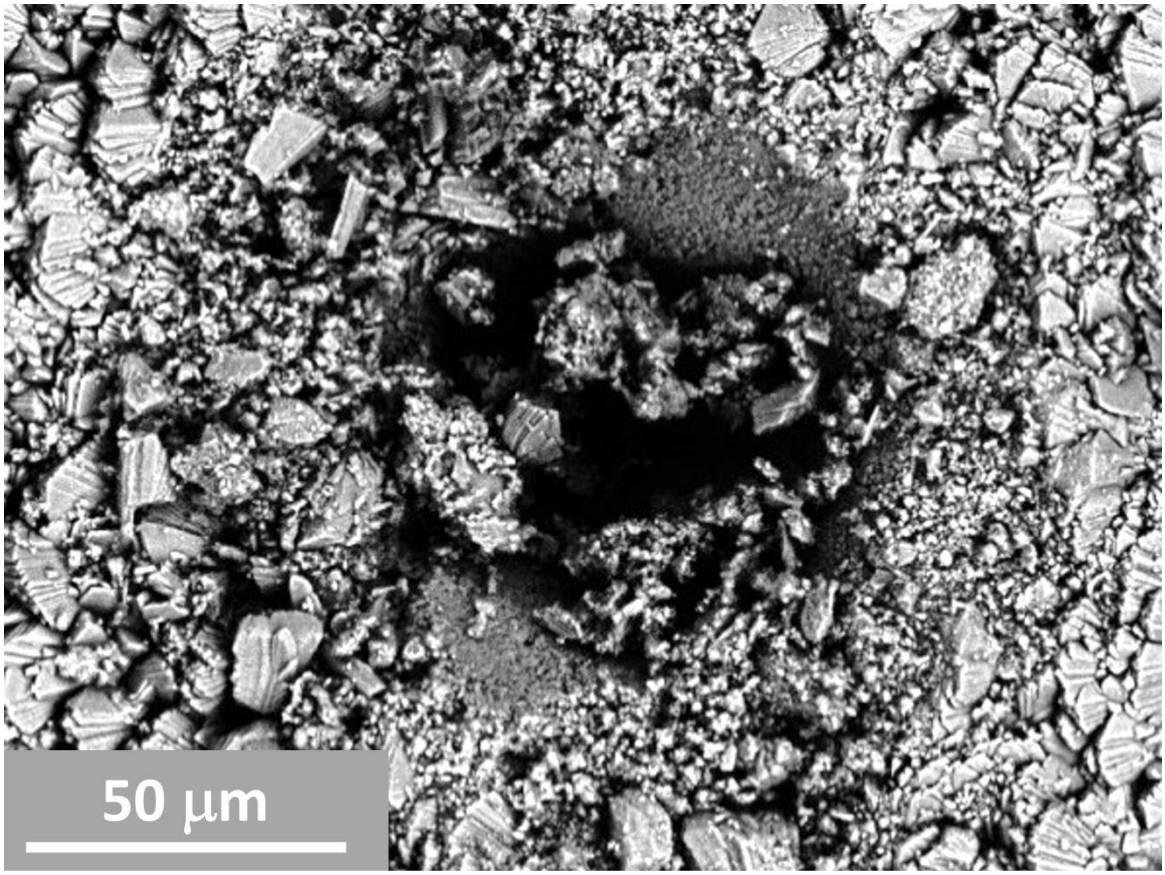
8(c).



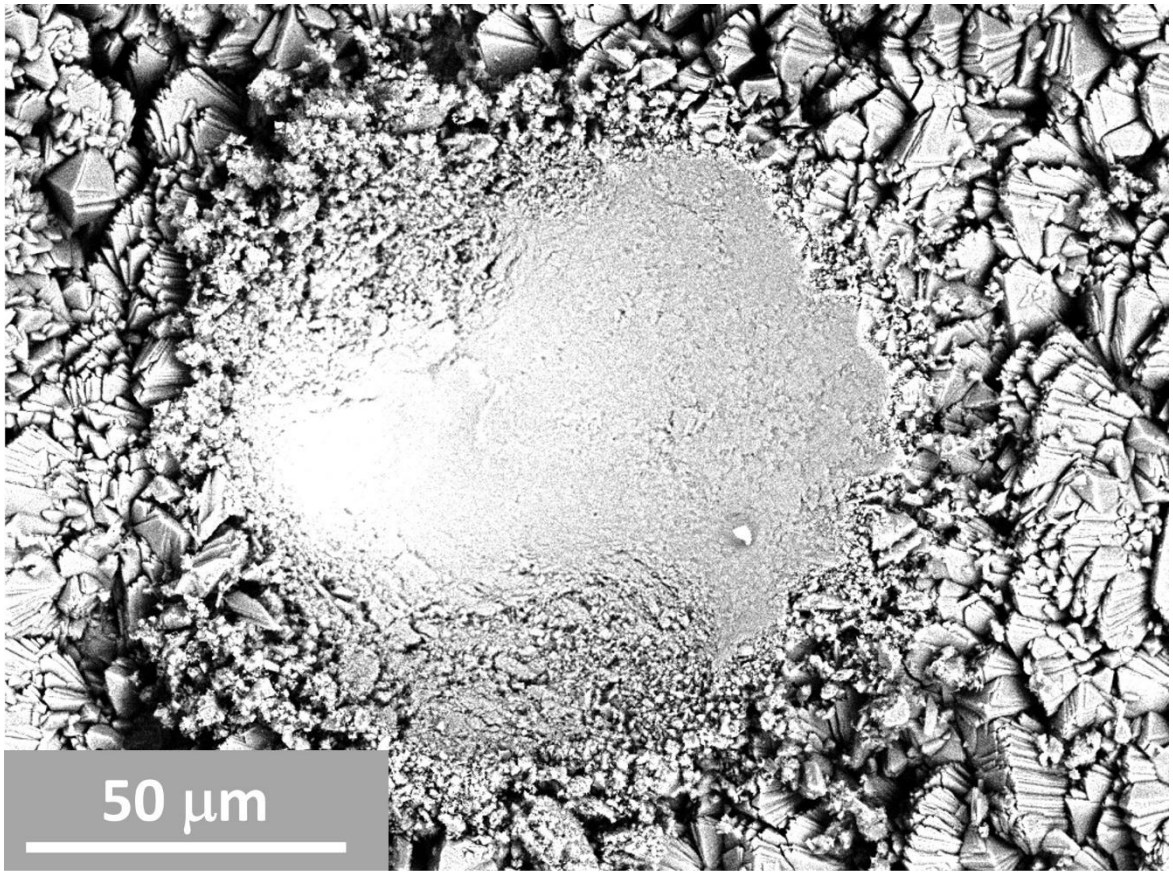
8(d)



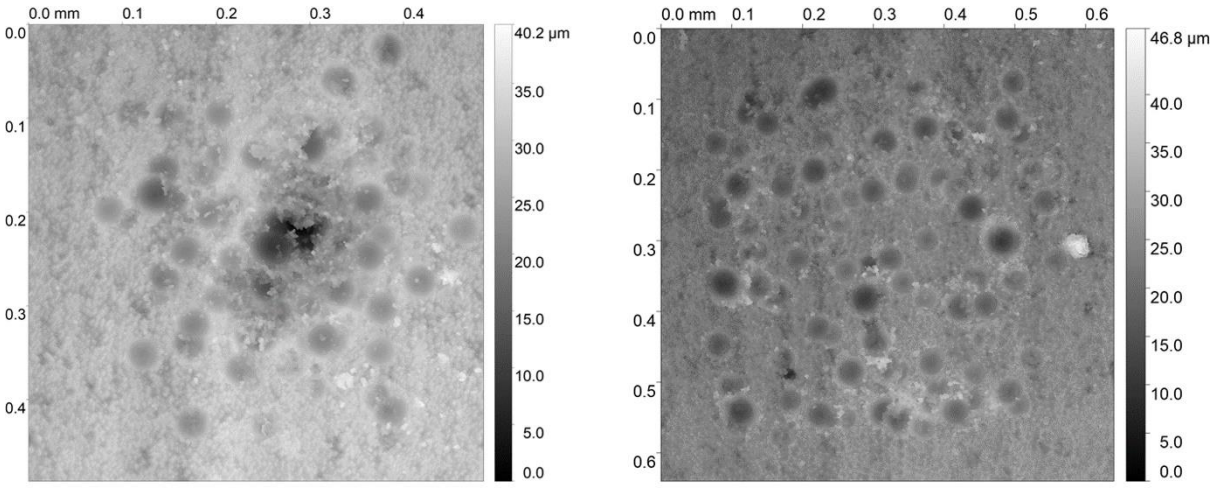
8(e)



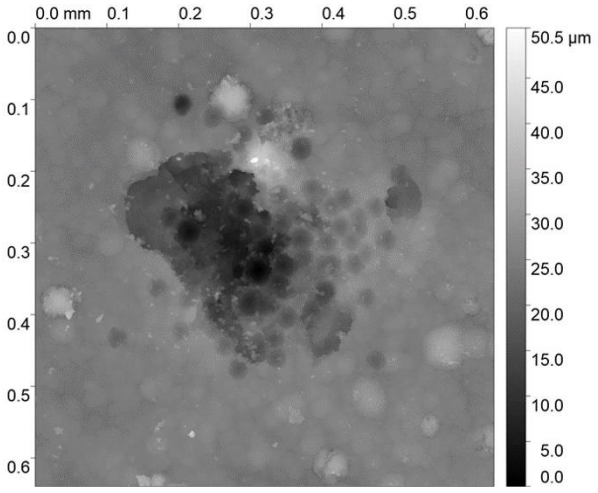
8(f)


50 μm

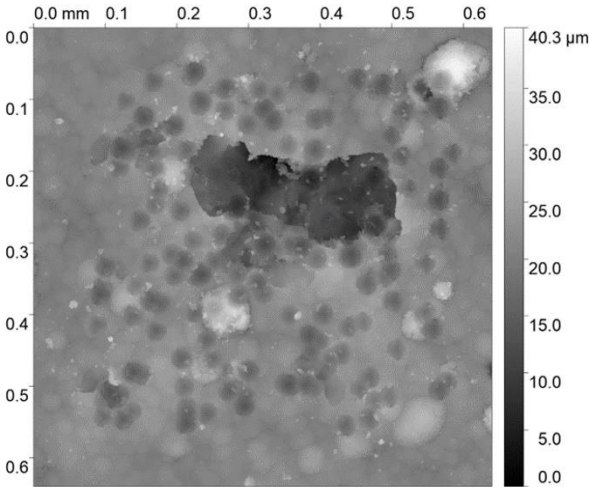
8(g)


0.0 mm 0.1 0.2 0.3 0.4
0.0
0.1
0.2
0.3
0.4
40.2 μm
35.0
30.0
25.0
20.0
15.0
10.0
5.0
0.0
0.0 mm 0.1 0.2 0.3 0.4 0.5 0.6
0.0
0.1
0.2
0.3
0.4
0.5
0.6
46.8 μm
40.0
35.0
30.0
25.0
20.0
15.0
10.0
5.0
0.0

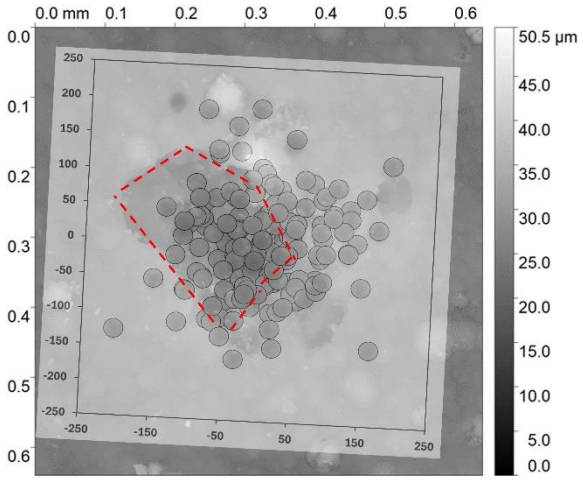
(a) (b)


0.0 mm 0.1 0.2 0.3 0.4 0.5 0.6
50.5 µm
45.0
40.0
35.0
30.0
25.0
20.0
15.0
10.0
5.0
0.0

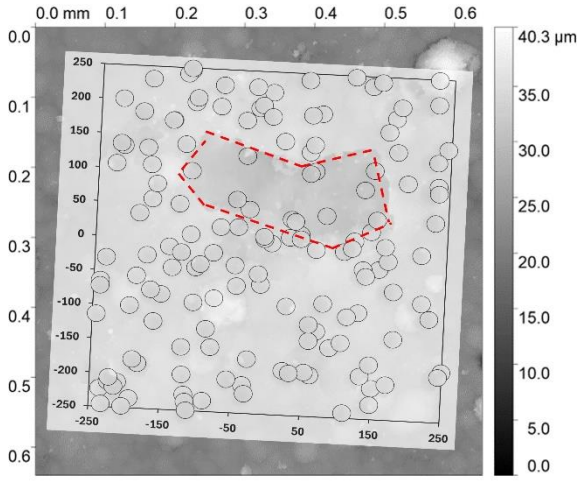
(c)


0.0 mm 0.1 0.2 0.3 0.4 0.5 0.6
40.3 µm
35.0
30.0
25.0
20.0
15.0
10.0
5.0
0.0

(d)

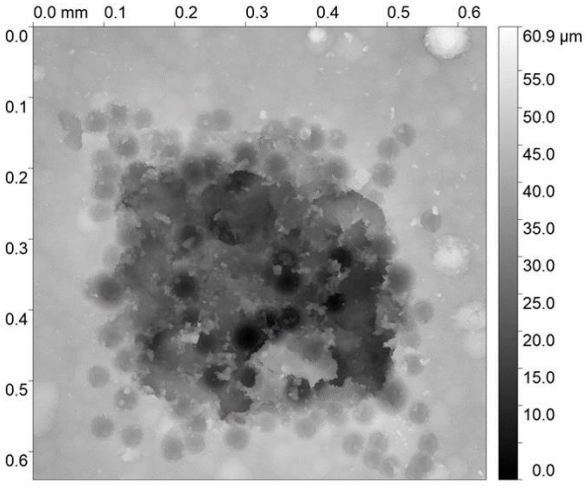

0.0 mm 0.1 0.2 0.3 0.4 0.5 0.6
50.5 µm
45.0
40.0
35.0
30.0
25.0
20.0
15.0
10.0
5.0
0.0

(e)

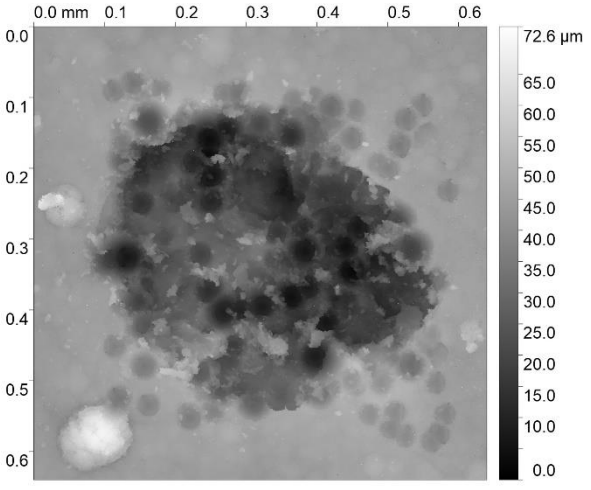

0.0 mm 0.1 0.2 0.3 0.4 0.5 0.6
40.3 µm
35.0
30.0
25.0
20.0
15.0
10.0
5.0
0.0

(f)

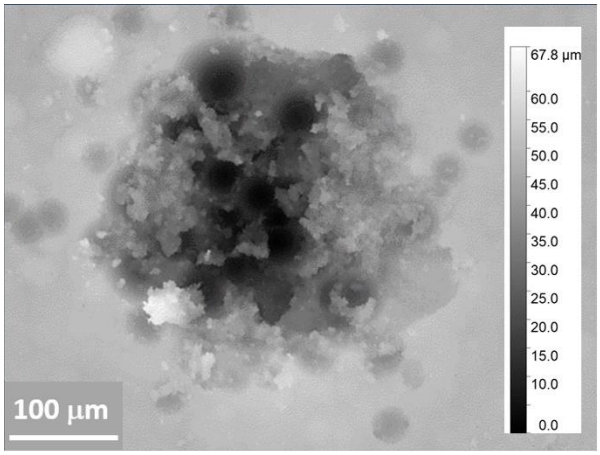
9.


0.0 mm 0.1 0.2 0.3 0.4 0.5 0.6
60.9 µm
55.0
50.0
45.0
40.0
35.0
30.0
25.0
20.0
15.0
10.0
0.0

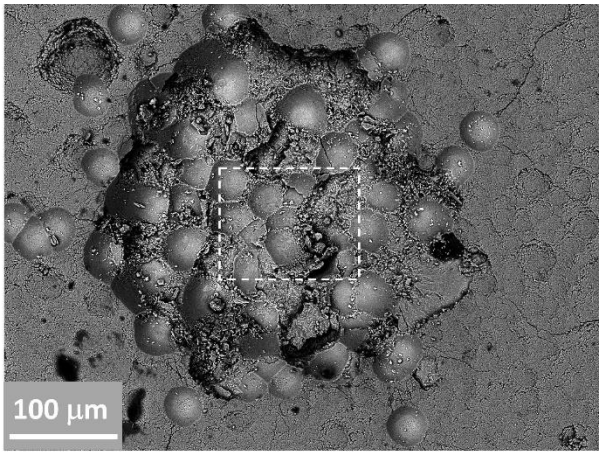
(a)


0.0 mm 0.1 0.2 0.3 0.4 0.5 0.6
72.6 µm
65.0
60.0
55.0
50.0
45.0
40.0
35.0
30.0
25.0
20.0
15.0
10.0
0.0

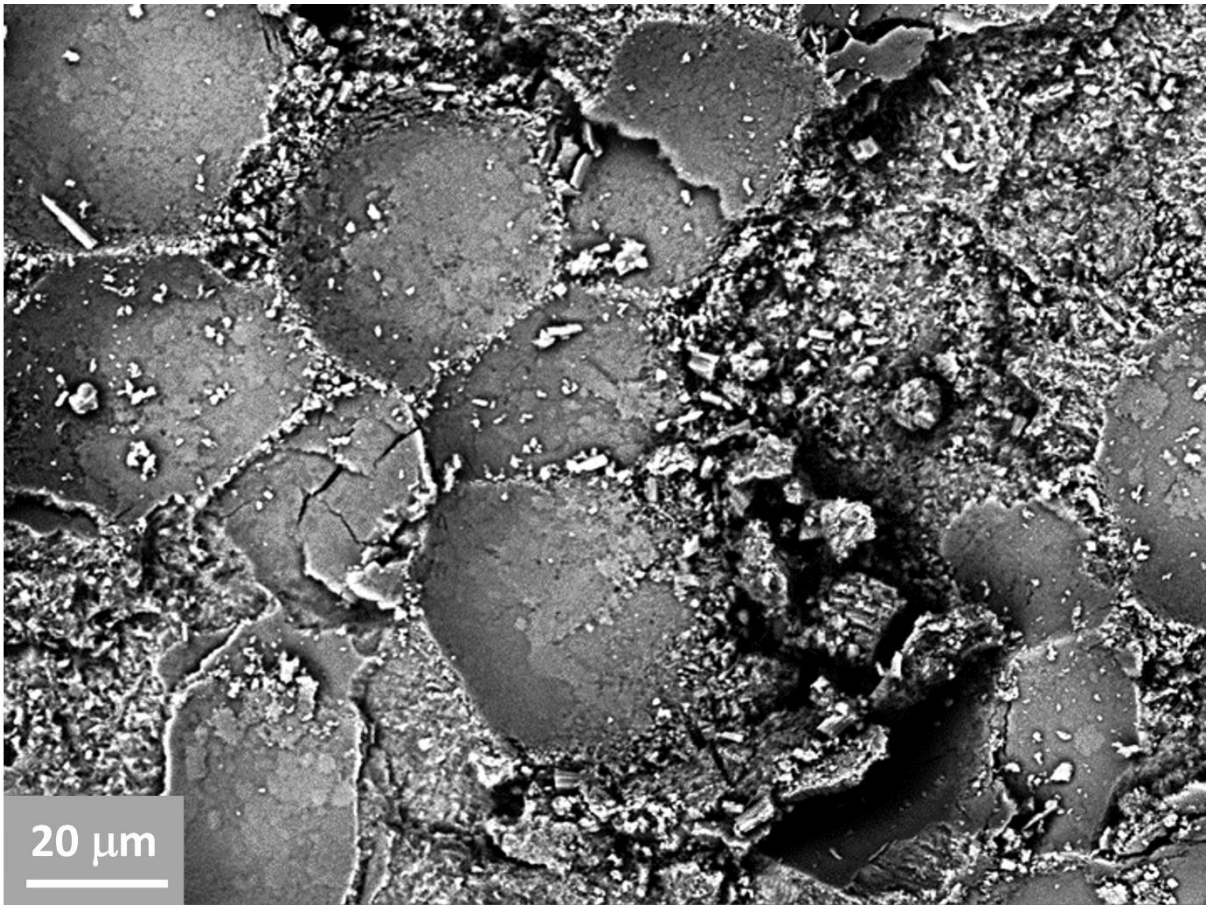
(b)


67.8 µm
60.0
55.0
50.0
45.0
40.0
35.0
30.0
25.0
20.0
15.0
10.0
0.0
100 µm

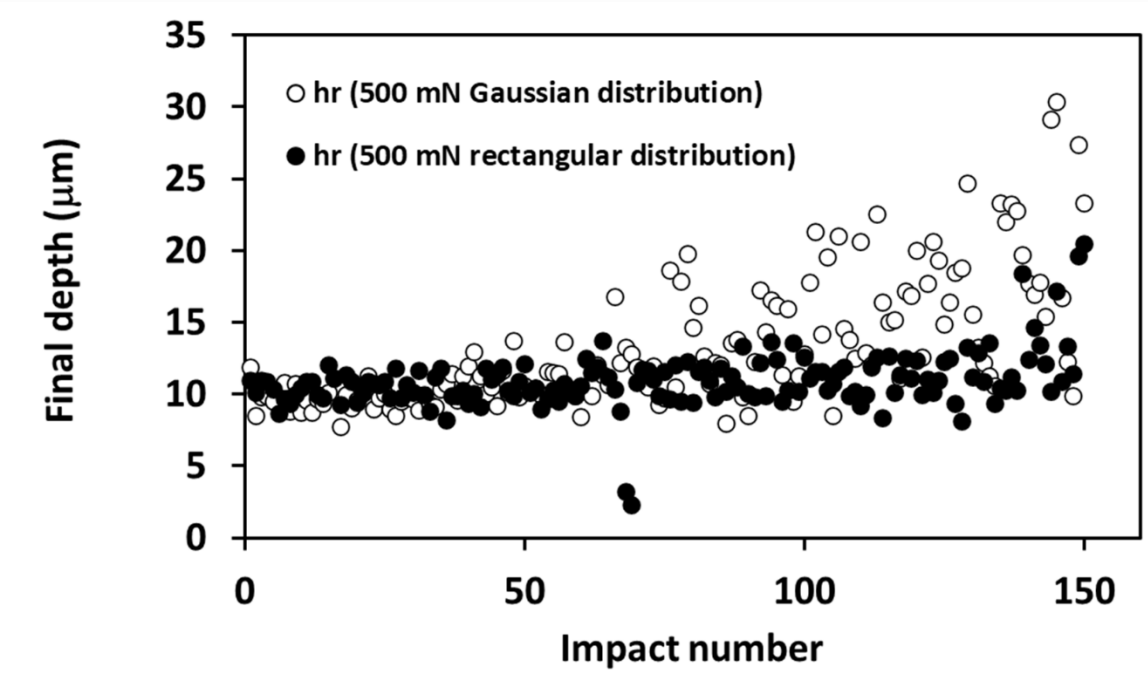
(c)


100 µm

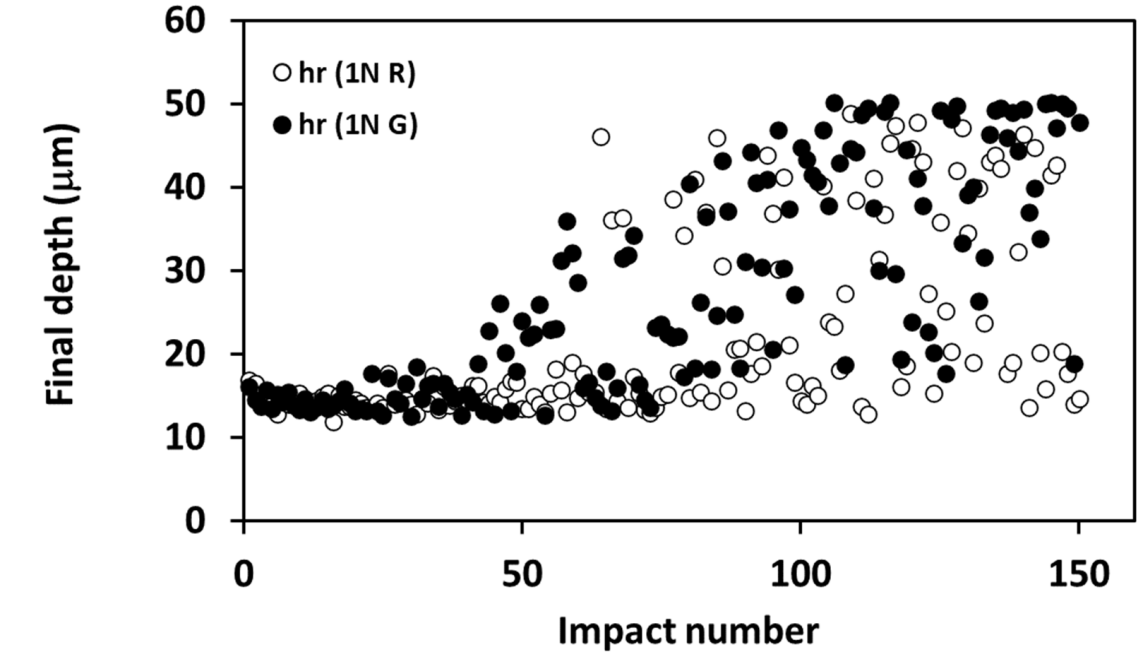
(d)


20 µm

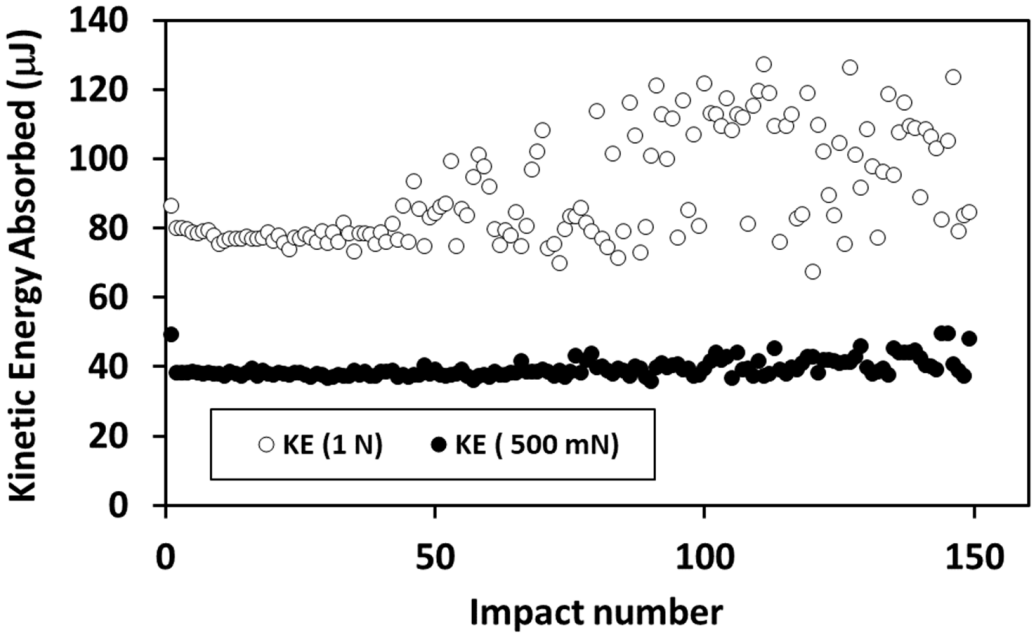
10(e).


hr (500 mN Gaussian distribution)
hr (500 mN rectangular distribution)
Final depth (μm)
Impact number
0
5
10
15
20
25
30
35
0
50
100
150

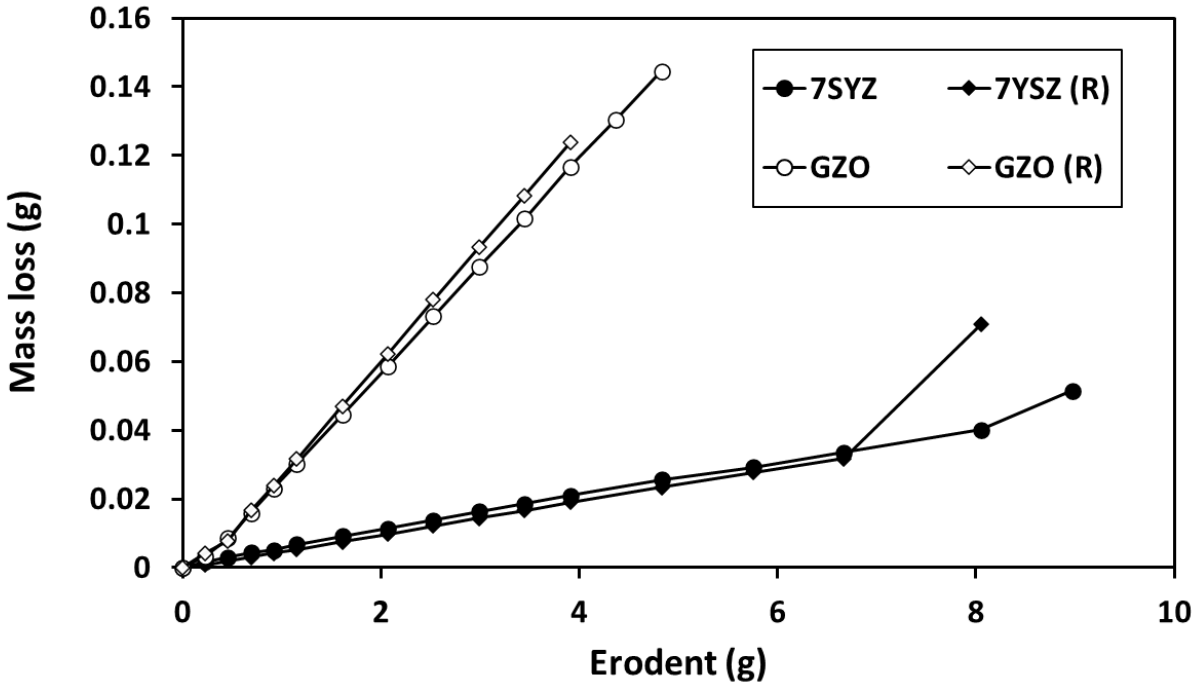
11(a).


hr (1N R)
hr (1N G)
Final depth (μm)
Impact number
0
10
20
30
40
50
60
0
50
100
150

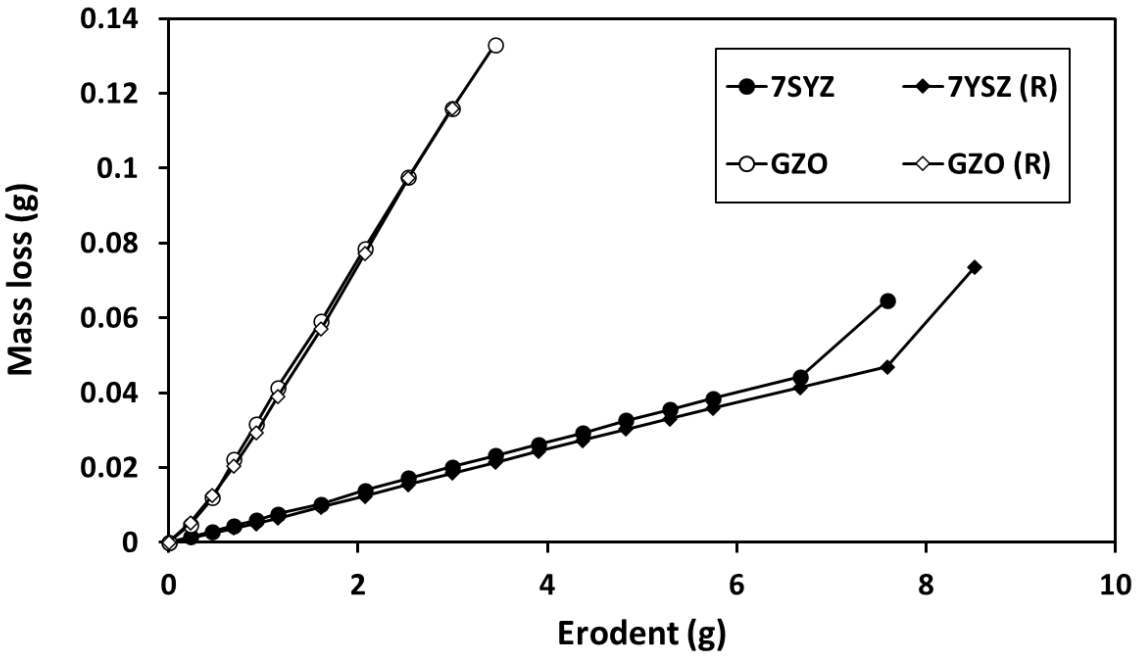
11(b).


Kinetic Energy Absorbed (μJ)
140
120
100
80
60
40
20
0
0
50
100
150
Impact number
KE (1 N)
KE (500 mN)

11(c).


Mass loss (g)
0.16
0.14
0.12
0.1
0.08
0.06
0.04
0.02
0
0
2
4
6
8
10
Erodent (g)
7SYZ
7YSZ (R)
GZO
GZO (R)

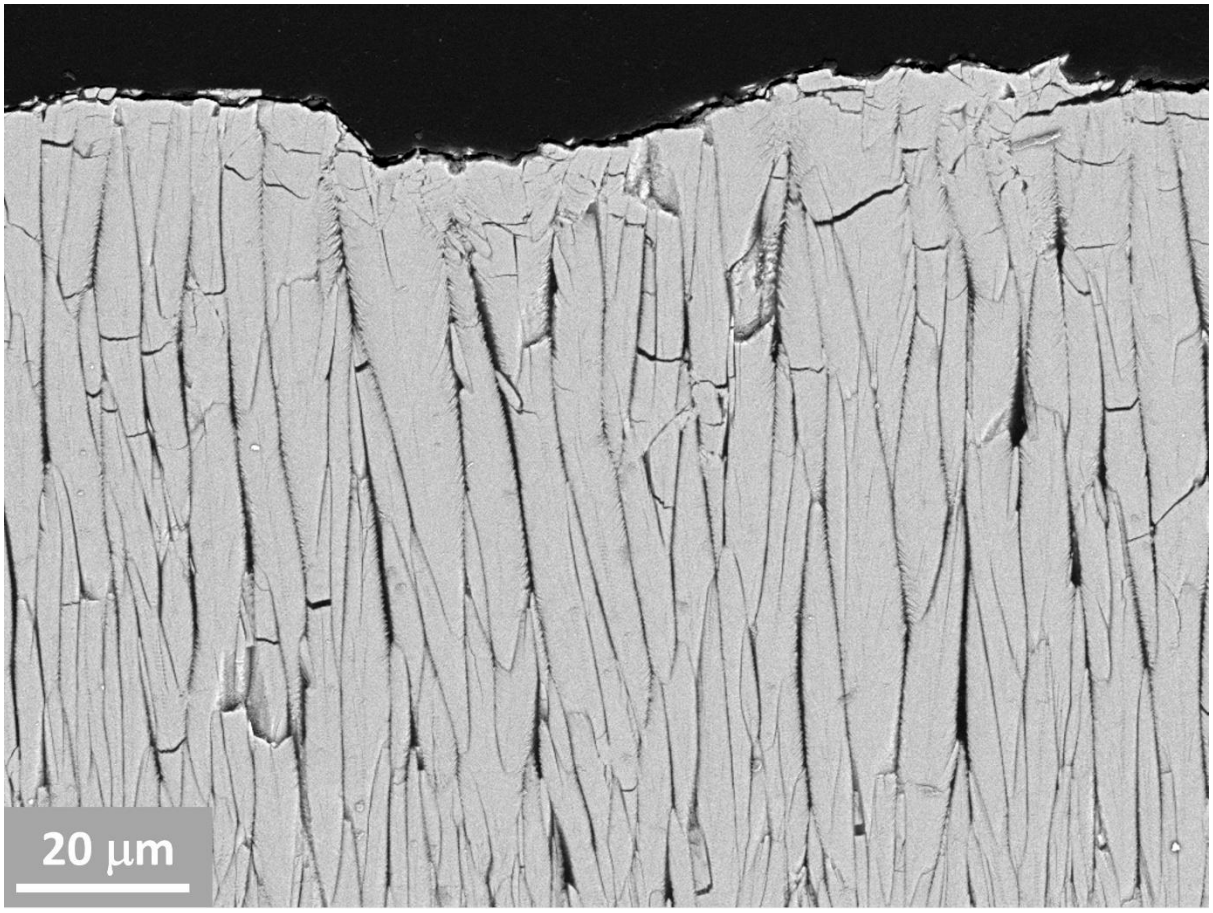
12(a).


0.14
0.12
0.1
0.08
0.06
0.04
0.02
0
Mass loss (g)
0
2
4
6
8
10
Erodent (g)
7SYZ
7YSZ (R)
GZO
GZO (R)

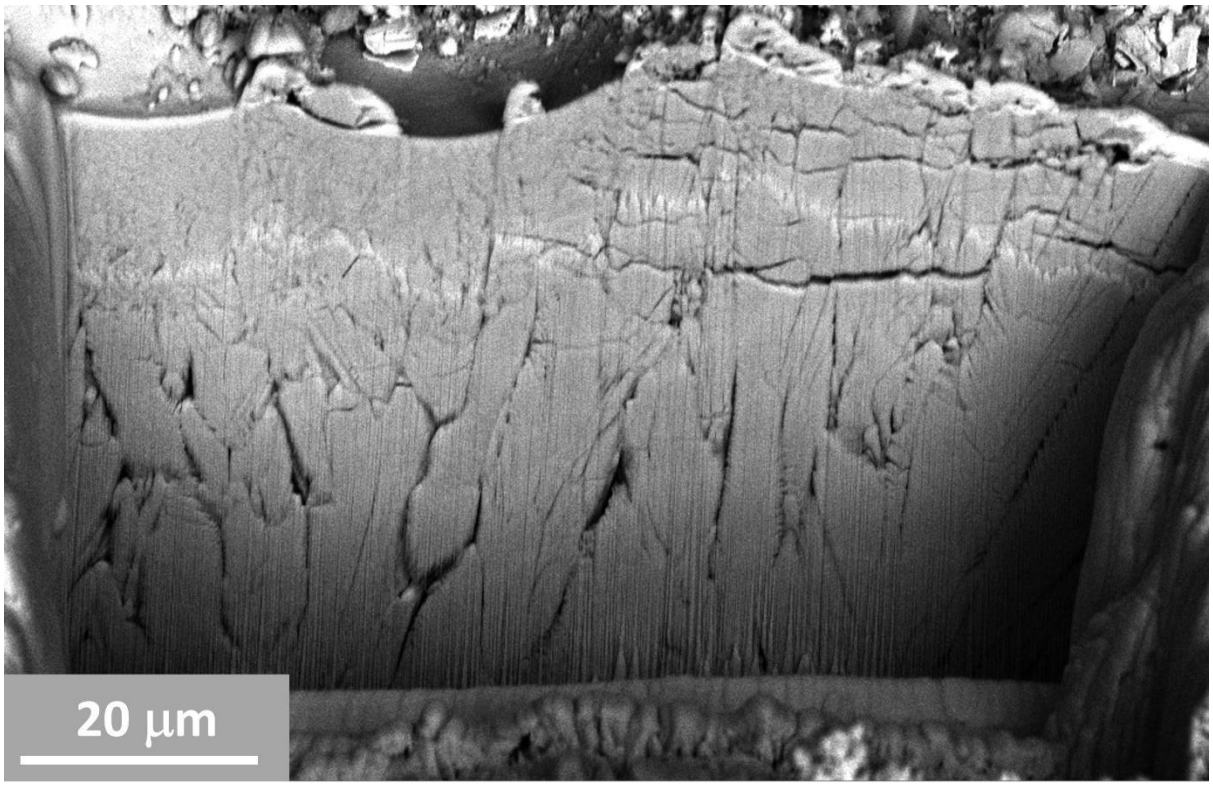
12(b).



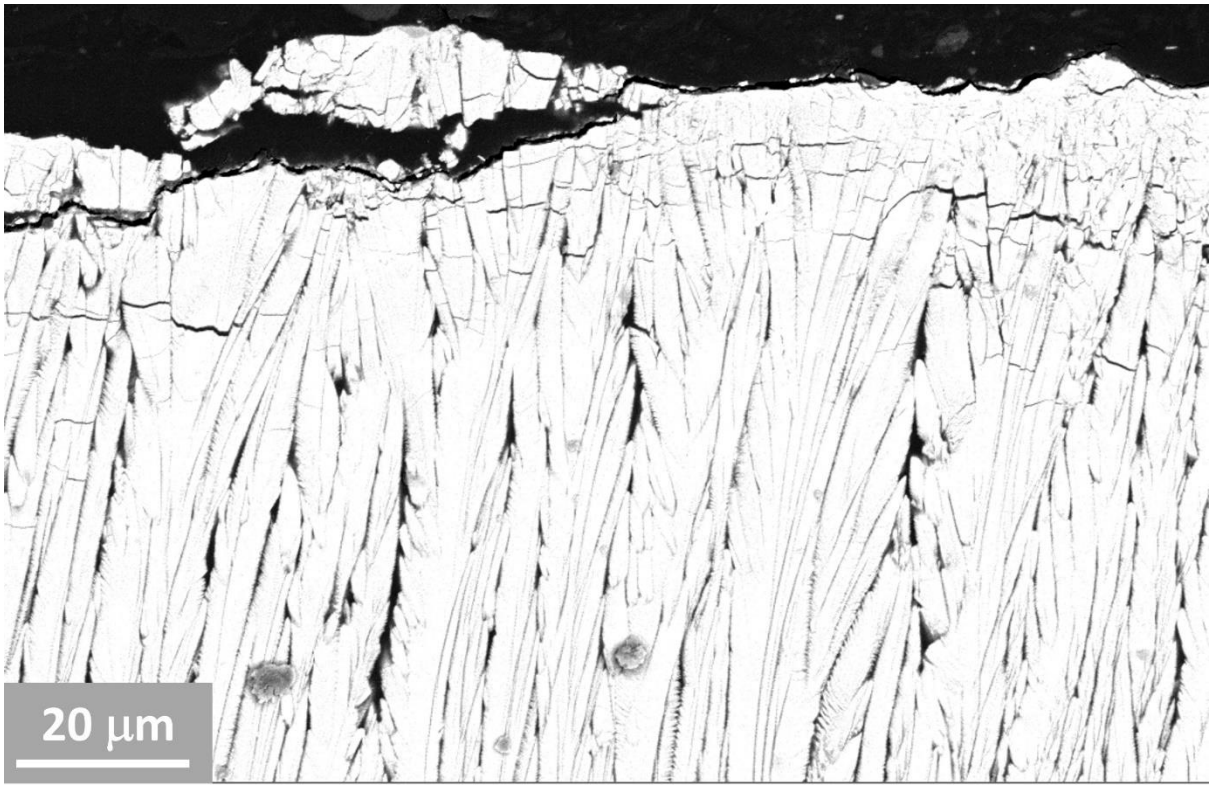
13(a)



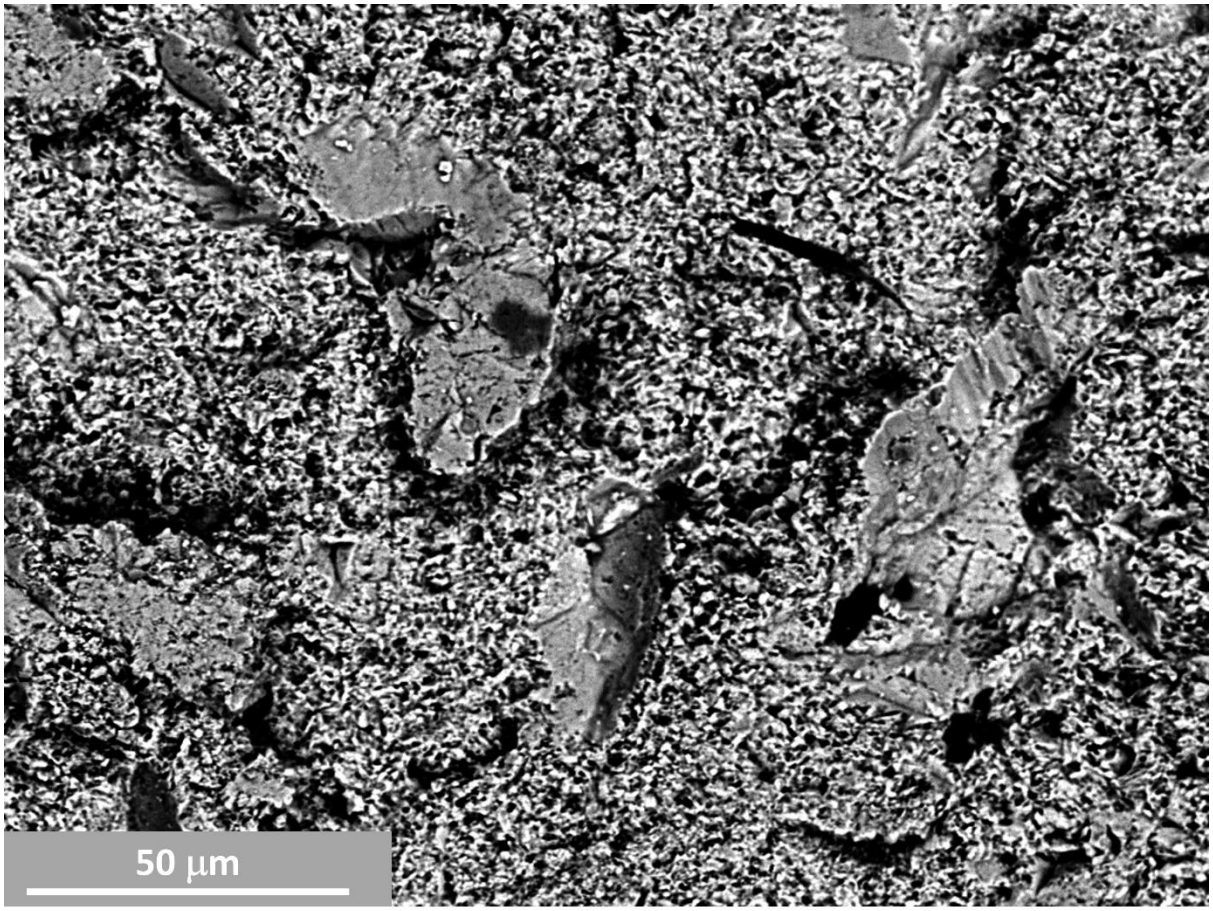
13(b)



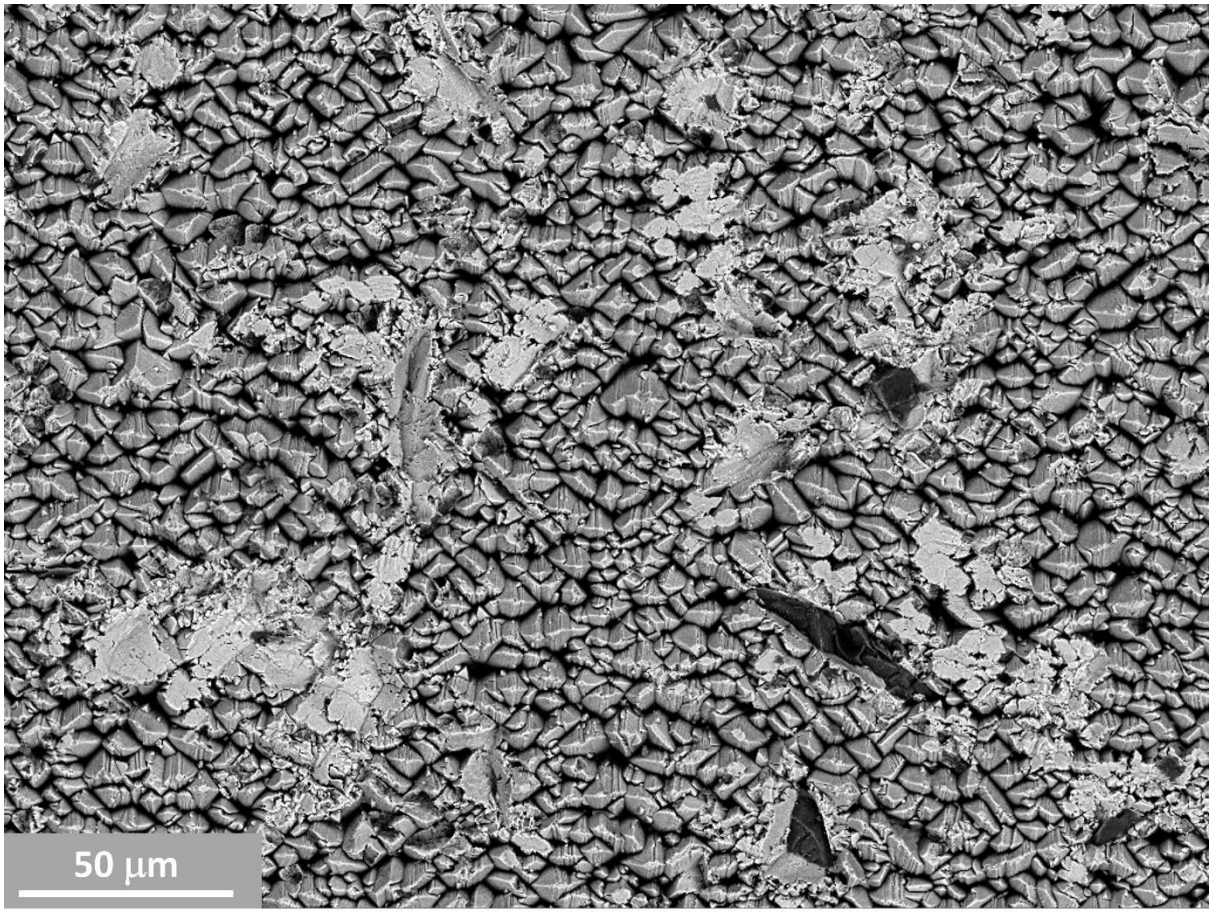
13(c)



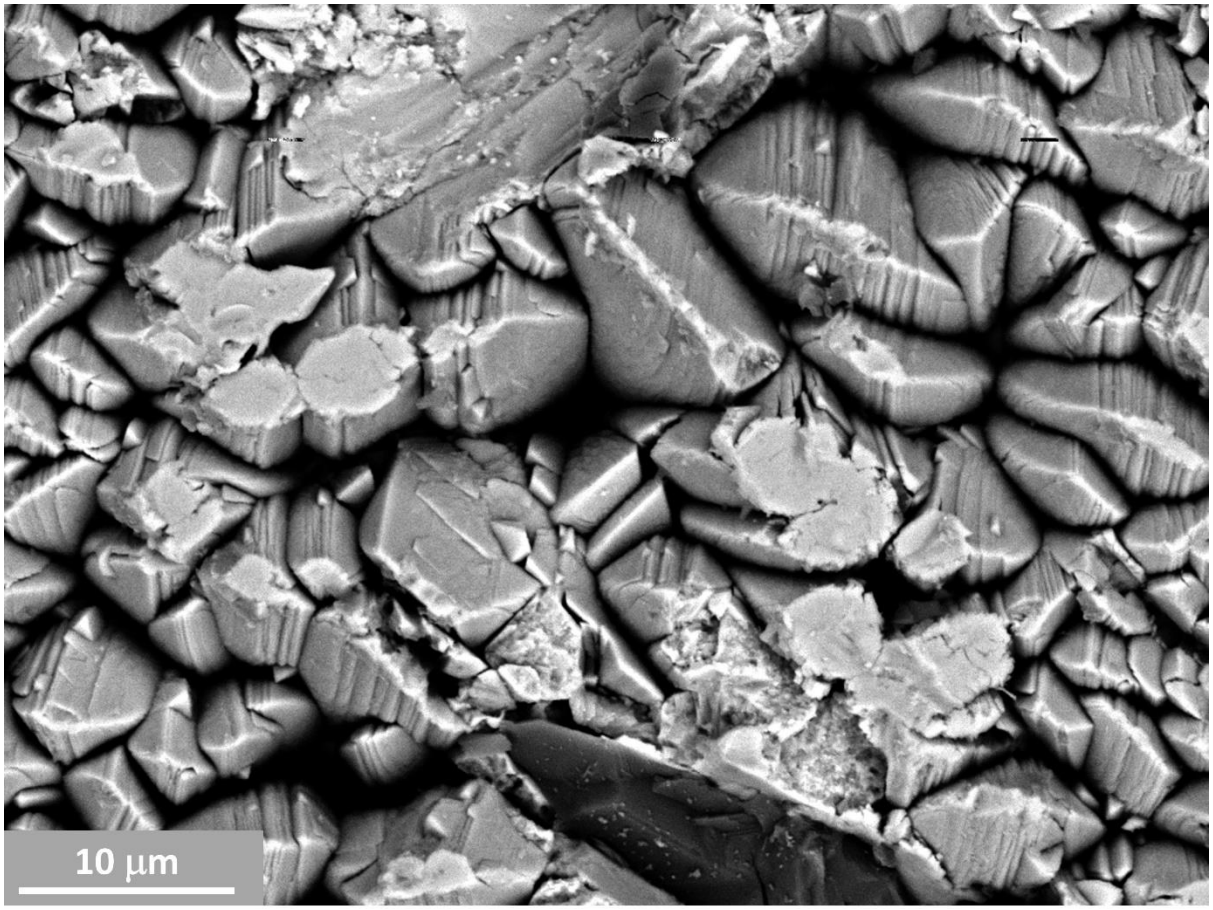
13(d)



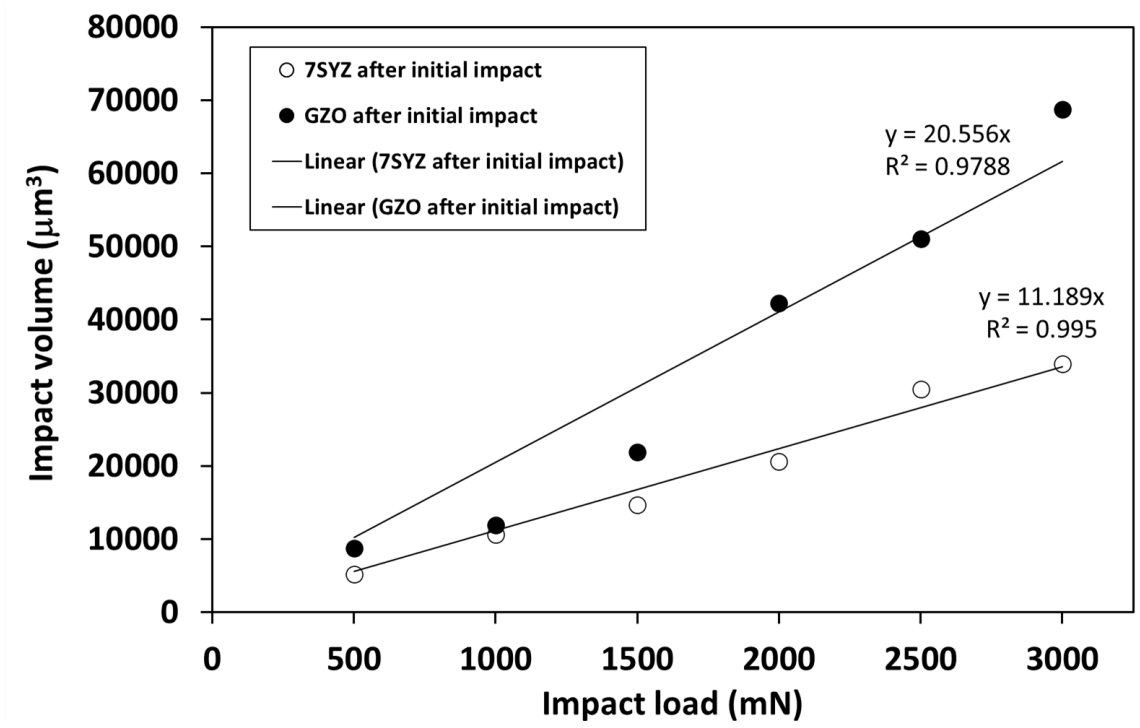
14(a).



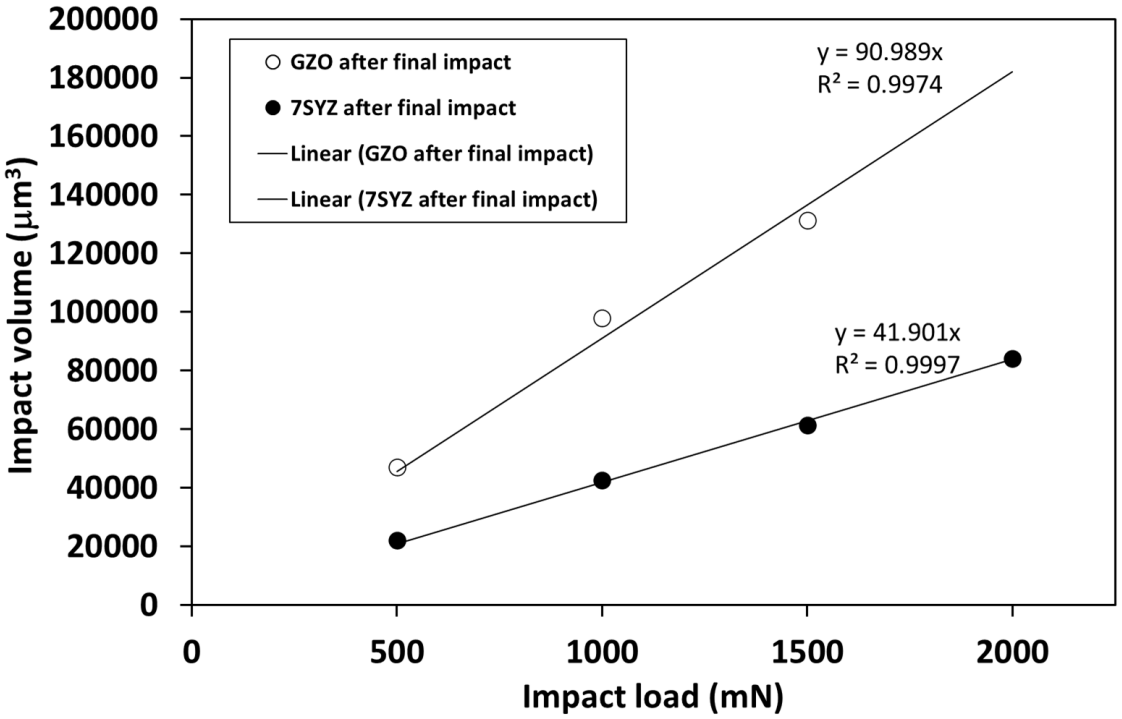
14(b).


10 μm

14(c).


7SYZ after initial impact
GZO after initial impact
Linear (7SYZ after initial impact)
Linear (GZO after initial impact)
y = 20.556x
R² = 0.9788
y = 11.189x
R² = 0.995
Impact volume (μm³)
Impact load (mN)
0
10000
20000
30000
40000
50000
60000
70000
80000
0
500
1000
1500
2000
2500
3000

15(a).


200000
180000
160000
140000
120000
100000
80000
60000
40000
20000
0
Impact volume (μm³)
0
500
1000
1500
2000
Impact load (mN)
GZO after final impact
7SYZ after final impact
Linear (GZO after final impact)
Linear (7SYZ after final impact)
y = 90.989x
R² = 0.9974
y = 41.901x
R² = 0.9997

15(b).



https://dspace.org/

Damage mechanisms in solid particle impact and erosion testing of thermal barrier coatings

Beake, Ben D.; Isern, Luis; Zhang, Hannah; Chalk, Christine; Goodes, Stephen R. ...

2025-12-01
Elsevier
https://doi.org/10.1016/j.surfcoat.2025.132844
Beake BD, Isern L, Zhang H, et al., (2025) Damage mechanisms in solid particle impact and erosion testing of thermal barrier coatings. Surface and Coatings Technology, Volume 517, December 2025, Article number 132844

Downloaded from a DSpace repository. https://dspace.org/